Additive manufacturing of binary alloys

A molecular dynamics study on laser powder bed fusion of TiAl

Master thesis

Kevin Vietz

Examiner: Prof. Dr. Johannes Roth
Co-Examiner: Prof. Dr. Hans Peter Büchler

Institute for Functional Matter and Quantum Technologies
University of Stuttgart, Germany
September 2023

Contents

Abbreviations

AM	Additive Manufacturing
CNA	(adaptive) Common Neighbor Analysis
fcc	face-centered cubic
hcp	hexagonal close packed
IMD	ITAP Molecular Dynamics
LPBF	Laser Powder Bed Fusion
MD	Molecular Dynamics
TiAl	Titanium Aluminide

1 Introduction and motivation

New applications in the field of *Additive Manufacturing (AM)* demand a constant increase in quality and productivity [1]. One way to achieve this is to use new, more sophisticated materials. *Titanium Aluminide (TiAl)* is an attractive material used in various domains, such as aerospace and automotive industries [2]. This is because TiAl based alloys have a low density combined with high specific yield strengths, high specific stiffness, good oxidation resistance and good creep properties up to high temperatures [3]. The most commonly used alloy is γ-TiAl as it is able to maintain its mechanical properties even at high temperatures [4]. However, because γ-TiAl is a typical intermetallic material, its properties make it difficult to process by conventional methods [5]. Therefore, one promising method for fabricating γ-TiAl workpieces is AM [6].

AM, commonly referred to as 3D printing, is the construction of three-dimensional objects, typically made layer by layer. Since AM is a general type of manufacturing, there are a lot of process methods it covers. This study focuses on *Laser Powder Bed Fusion (LPBF)*, which is typically used for AM of metals and metallic alloys. We investigate the processing by performing computational simulations. Depending on the particular simulation method used, there are many physical processes to cover. We address those physical processes by using *Molecular Dynamics (MD)* simulations, based on ab-initio interactions. Compared to continuum descriptions used for finite element methods [7], this require less assumptions and furthermore, enables to analyze structures, elemental distributions, and defects on an atomistic level. From these analyzes, knowledge can be gained about the influences of certain processing parameters and thus, about the causes of quality-reducing properties.

With this study we build on top of previous works which already showed the functionality of the implementation [8], but focused on the manufacturing of pure metals [9, 10]. However, due to their superior properties we extend previous knowledge by studying binary alloys and in particular, the Ti-Al-system. Furthermore, we investigate the suitability of functionalized powders, because they have the ability to improve mechanical properties and the processability with LSPB [11]. In particular, we study the suitability of coated cores for the Ti-Al-system by comparing different material distributions and find suitable coatings to decrease aluminium evaporation during processing. Furthermore, we enlarge previous systems in terms of the number of powder grains to have a meaningful system that resembles real powder. Hence, we are able to study melt pool behavior and have a foundation to further investigate the correlations to real processing parameters.

The remainder of the thesis is organized as follows. Chapter 2 covers the fundamentals of AM and how we depict the LPBF process in our computer simulations. Chapter 3 discusses the methodological instruments we use to produce and analyze results. Chapter 4 contains the results and evaluation for our simulations. Finally we discuss the results in chapter 5 and give conclusions in chapter 6.

2 Theoretical background

This chapter presents important background. Section 2.1 covers the theory about LPBF. In particular we explain the functionality of LPBF and correlated fundamentals. Section 2.2 is dedicated to the reflectance of metals and introduces a simple approach to have reasonable arguments for neglecting the angular dependency of the reflectance. Finally, section 2.3 describes the computational implementation of LPBF, showing how the highly non-linear material dynamics can be simulated.

2.1 LPBF

LPBF, also known as selective laser melting, is a technology for the AM of metals and metallic alloys. Instead of fused filament fabrication, which already made their way to private homes [12], it uses a powder bed based source for the additive process. The laser is used to melt and fuse the metallic powders together.

This section starts with an introduction about LPBF in section 2.1.1 followed by an approach to correlate different processing parameters for scaling purposes in section 2.1.2. Melting modes are explained in section 2.1.3 which are different regimes in terms of energy density. Finally, section 2.1.4 explains different defects and how they arise, as well as how they can be observed in atomic simulations.

2.1.1 Technical functionality of LPBF

The scheme of the LPBF manufacturing process is sketched in figure 2.1. It shows two powder containers, as well as two pistons, a coating unit in form of a roll, the laser-scanner unit and the fabricated object within the fabrication containers. At first the fabrication piston on the right is lowered to have enough space for a layer of powder. Then, the delivery piston on left lifts the powder in the storage which is transported to the fabrication container and applied as new layer by the coating unit. Finally, the laser beam is directed onto the printing plane and scans the desired structure. Thereby, the metal powder fuses onto the already manufactured object. By repeating this procedure, the object is fabricated layer by layer.

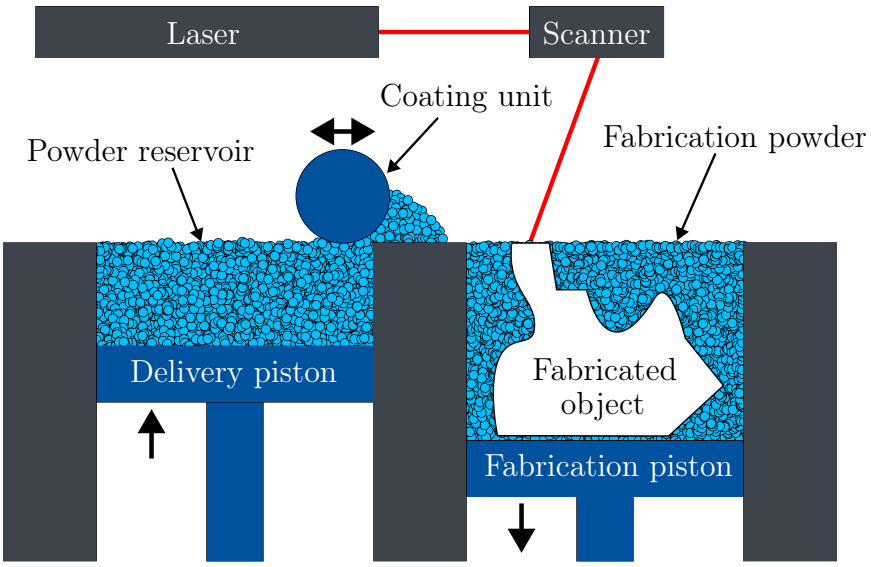

Figure 2.1: Scheme of the LPBF manufacturing process.

2.1.2 Scaling behavior of laser-weld properties

Different laser systems need different processing parameters. Therefore, it is necessary to have good predictions in the correlations between important values such as velocity, power and material properties. This section derives the normalized enthalpy which is commonly used for the translation of processing parameters. For a deeper insight into this topic one can read the work of Hann, Iammi, and Folkes [13] which was used for subsequent explanations.

At first we take the dimensionless welding depth δ^* which is normalized by the half-width of a Gaussian beam

$$\delta^* = \frac{\delta}{2\sigma} \tag{2.1}$$

and relate this to laser parameters by

$$\delta^* = fn\left(B \cdot \frac{P}{\sqrt{\sigma^3 v}}\right), \tag{2.2}$$

where P is the laser power, v the speed of weld and B a normalization constant [14]. As B has the dimension $[\mathrm{J}^{-1}\mathrm{m}^2\mathrm{s}^{1/2}]$ and by the introduction of a dimensionless constant C one can write

$$\boldsymbol{B} = \frac{\mu C}{\rho h_\mathrm{S} \sqrt{\alpha}} \tag{2.3}$$

with μ being the absorptivity of the surface, ρ the density of the material, h_S the enthalpy at melting and α the thermal diffusivity. Combining this with equation (2.2), we can suggest the dimensionless melting depth to relate to laser parameters, as well as material

parameters by

$$\delta^* = fn\left(\frac{\mu CP}{\rho h_S \sqrt{\sigma^3 \alpha v}}\right). \tag{2.4}$$

By introducing the enthalpy

$$\Delta H = \frac{\mu CP}{\rho\sqrt{\sigma^3 \alpha v}} \tag{2.5}$$

one can rewrite (2.4) as

$$\delta^* = f\left(\frac{\Delta H}{h_S}\right). \tag{2.6}$$

Hence, the dimensionless melting depth is a function of the normalized enthalpy $\Delta H/h_S$. This matches the physical interpretation that the material will neither melt nor evaporate if the local enthalpy is not large enough for a phase change. However, for our use case we are mainly interested in the correlation between laser parameters. Therefore, we can use the normalized enthalpy to have a ratio between laser power P and welding speed v as

$$\frac{P}{\sqrt{v}} = \frac{\Delta H \rho \sqrt{\sigma^3 \alpha}}{h_S \mu C}. \tag{2.7}$$

2.1.3 Melting modes

A thorough knowledge of controlling the melting pool geometry is important to prevent defects during LPBF. Based on the work of Patel and Vlasea [15] this section gives a brief overview of the different melting modes in LPBF.

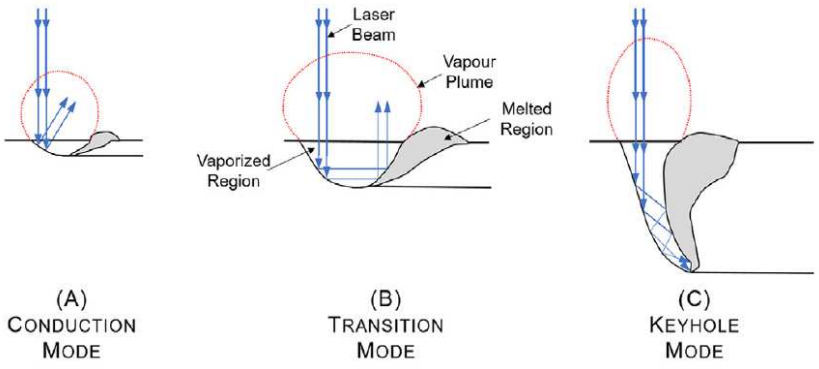

Figure 2.2: An illustration of different melting modes in terms of vaporized region shape [15].

In LPBF, three different melting modes can be employed, namely *conduction*, *transition* and *keyhole* mode [15]. Figure 2.2 illustrates the different modes and compares their vaporized region shapes, which is a crucial factor to the number of laser beam reflections. Depending on the processing conditions in LPBF, a distinction can essentially be made between conduction and keyhole mode. Conduction mode arises if the power density

undergoes a certain threshold and therefore the underlying heat transfer mechanism is dominated by heat conduction. Keyhole mode on the other side is observed if this threshold exceeds. The intense localized heating and vaporization causes the forming of a deep vapor cavity within the molten metal. For keyhole mode, the heat transfer mechanism within the melting pool is dominated by convective heat transfer.

The transition mode, which is also shown in figure 2.2 is a regime between conduction and keyhole mode. It shows characteristics of conduction, as well as of keyhole mode. To differentiate between different modes the extent and depth of vaporization can be used as a threshold. Typically, vaporization can be observed in all melting modes, but due to the powder density threshold mentioned earlier, conduction mode is considered to generate least vaporization. For conduction mode melting it even is considered to be negligible [15, 16].

In the case of titanium we assume to have a low reflectivity and hence expect high front vaporization wall angles. The beam reflection would therefore be outside of the keyhole and hence, conduction mode would be observed. Unless the heat input is increased to such an extent that a certain threshold is exceeded, small front vaporization wall angles would lead to multiple reflections and eventually form of a keyhole. However, Aluminium has a high reflectivity compared to titanium. Due to the high reflectivity and high thermal conductivity the melting progresses rapidly after it started. Therefore, the transition range for aluminium between conduction and keyhole mode welding is rather small compared to titanium.

2.1.4 Defects

There are a lot of factors which influences the quality of the manufactured object. Hence, there are a lot of defects which can be arise in LPBF. For example, thermal stresses inside the material can lead to the formation of cracks [17]. This section discusses porosities, which are among the most common type of defects. In the following, two types of porosities are discussed, namely *lack of fusion* and *keyhole* porosities.

Lack of fusion is a porosity defect that arise when there is no complete adherence of the melt to underlying substrate or surrounding part. For example, this defect occurs if the hatch spacing is too large causing the energy supply to be insufficient. Typically, the porosities are relatively big.

Figure 2.3a depicts an example of pores caused by the lack of fusion. The pores are shaped irregularly and reach lengths of 450 µm. The size and irregular shape of the pores have a large impact on the quality of the manufactured component, as they can lead to unwanted cracks in the material [18].

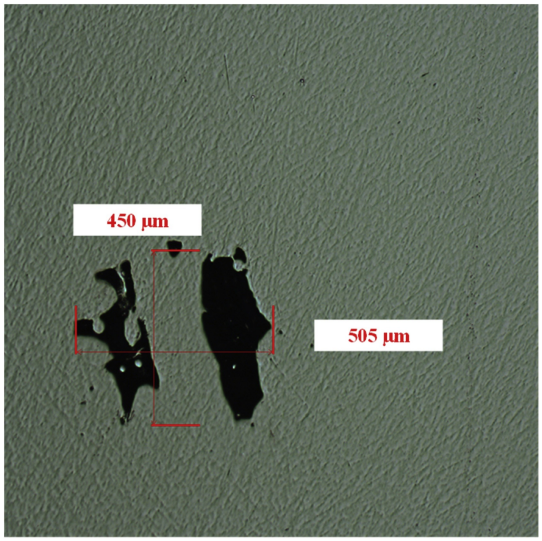

(a) Lack of fusion pores [18].

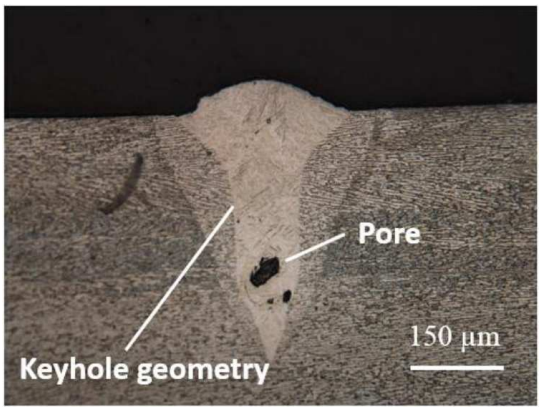

(b) Keyhole geometry and pore [19].

Figure 2.3: Examples of porosities caused by the lack of fusion and keyholing.

Keyholing is an effect that has already been introduced as being one of the melting modes which were explained in section 2.1.3. They arise if a certain energy density threshold is exceeded. The intense heating vaporizes material such that it causes the forming of a deep vapor cavity. The shape favors the reflection within the cavity as shown in figure 2.2c and increases the depth of the cavity even further. This leads to a shape as shown in figure 2.3b. The geometry of the cavity is relatively wide in the upper part, has a constant width in the middle area and then narrows to a point at the bottom. The example in figure 2.3b shows that a pore has formed in the lower part of the keyhole. This may be attributed to the vaporization of material and trapping of gas bubbles by melted material.

The observation of pores in our simulations is not an easy task because it requires certain requirements. Figure 2.4 shows the typical trend of part porosities. We can see that there are in general three regions, separated from each other by a certain threshold in the scan speed, respectively in the energy density. Those are visualized by the dashed vertical lines. The increase of keyhole and lack of fusion porosities goes along with previous considerations. In between the thresholds is a range, where the manufactured part is most dense. This area needs to be captured in order to prevent porosities and increase parts quality.

The lack of fusion can be observed in atomistic simulations as shown in previous works [9, 10]. Since vacuum cavities tend to vanish over time, a protective gas has to be integrated to the simulations. A first attempt to simulate LPBF with argon has already been made and is currently under development [10, 21]. Nevertheless, we will see in section 4.3.5 that lack of fusion porosities can also be observed in molecular dynamics

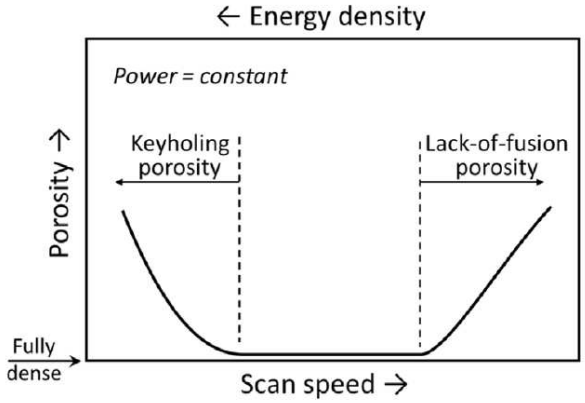

Figure 2.4: Typical porosity trend in terms of scan speed and energy density [20].

simulations in vacuum if there is a certain stabilizing environment.

Although lack of fusion is easily observable in MD simulations, the porosities which arise from keyholing face completely different challenges. As mentioned, there are a lot of reflections which favors the formation of a keyholes if the energy density exceeds a certain threshold. However, in the performed simulations, there is no ray tracing included and thus, reflections as well as refractions are not taken into account. There is also the restriction of sample size in terms of computational effort which also hinders the observation of keyholing, although it would be possible to enlarge the necessary size and increase the energy density correspondingly.

2.2 Reflectance

This sections covers the fundamentals about reflectance. We also treat the reflectances of titanium and aluminium and introduce an approach to neglect the angular dependency in our simulations.

Definition *Reflectance is the ratio of reflected to incident electromagnetic power.*

Snell's law is used to describe the relation between incident angle θ_i and refractive angle θ_t in terms of waves passing through a boundary between two media. The relation depends on the media's refractive indices n_1 and n_2 and reads

$$n_1 \sin\theta_\mathrm{i} = n_2 \sin\theta_\mathrm{t}. \tag{2.8}$$

To derive an angle dependent reflectance we use the well known Fresnel equations [22]. For that we have to separate between s- and p-polarized components and yield the corresponding reflectances

$$R_\mathrm{s} = \left|\frac{n_1\cos\theta_\mathrm{i} - n_2\cos\theta_\mathrm{t}}{n_1\cos\theta_\mathrm{i} + n_2\cos\theta_\mathrm{t}}\right|^2 \quad \text{and} \quad R_\mathrm{p} = \left|\frac{n_1\cos\theta_\mathrm{t} - n_2\cos\theta_\mathrm{i}}{n_1\cos\theta_\mathrm{t} + n_2\cos\theta_\mathrm{i}}\right|^2. \tag{2.9}$$

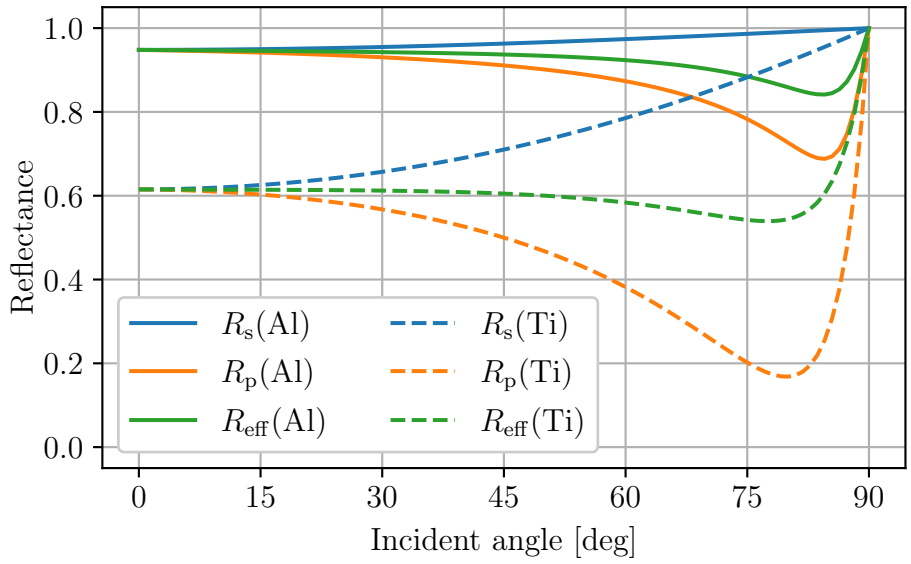

Figure 2.5: The reflectances for vacuum to aluminium, respectively titanium.

We can get rid of θ_t by using Snell's law (2.8) and use the averaged value of both reflectances to have an effective reflectance for unpolarized light

$$R_{\text{eff}} = \frac{R_s + R_p}{2}. \tag{2.10}$$

Figure 2.5 shows the calculated reflectances for light traveling from vacuum to aluminium, respectively titanium in dependence of the incident angle. For the calculations we used the complex refractive indices listed in table 2.1.

Table 2.1: Complex refractive indices for a wavelength of $\lambda = 1068\,\text{nm}$ [23–25].

Material	refractive index
Aluminium	$1.3818 + \text{i}10.035$
Titanium	$3.4712 + \text{i}4.0104$

Both reflectance calculations in figure 2.5 showing a similar behavior. For an incident angle of 0° they start at a certain reflectance and reach maximum reflectance at 90°. The reflectances of s-polarized light steadily increase with the incident angle, whereas the p-polarized and the effective reflectances first dip into a minimum before increasing to reach maximum reflectance. Despite a similar pattern, we see that aluminium has the higher reflectance, in particular for irradiation at 0°.

Although the reflectance cannot be neglected in LPBF, we would like to know whether one can neglect the angular dependence and therefore, make the simulations a lot easier and faster. We use spherical powder grains for our simulations and therefore, calculate

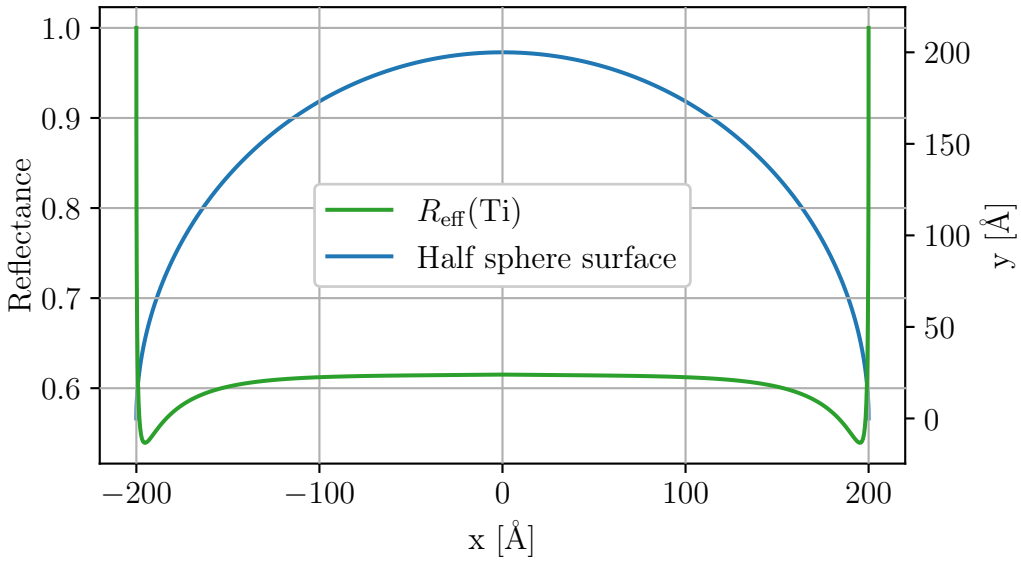

Figure 2.6: The effective reflectance for vacuum to titanium using incident angles at position x on a half sphere surface. The half sphere surface with a diameter of 400 Å is depicted in blue using the axis on the right.

.

the reflectance as before but for a half sphere. This is shown in figure 2.6 in two dimensions. The blue curve represents a half sphere surface of 400 Å in diameter. The green curve is, as before, the effective reflectance for vacuum to titanium, but now in dependence of the position on the half sphere surface.

As can be seen in figure 2.6, the change in reflection is only crucial at the very outside of the half sphere. This may lead to the assumption that the reflectance must not considered to be angle dependent. However, ignoring the incident angle might result in a loss of quality and must be considered carefully. In order to avoid loss of quality, ray tracing should be implemented.

2.3 Computational implementation

The goal is to perform numerical simulations to depict the highly non-linear material dynamics of a system under laser irradiation. At first, section 2.3.1 treats molecular dynamics, which is the used simulation method and based on the equations of motions. Afterwards section 2.3.2 covers the algorithms, namely integrators, that are used to integrate the equations of motion. In our simulations we limit atomic interactions to short ranges and use a common method for metals to describe them, which is described in sections 2.3.3 and 2.3.4. For the implementation of the laser irradiation section 2.3.5 explains the basic concept how to rescale the atom energies and includes also an

explanation of the implemented extension to the absorption coefficient. Finally, sections 2.4 covers some optimization methods we use to increase the computations efficiency.

2.3.1 Molecular dynamics

Molecular Dynamics (MD) is a method in computer simulations which is used for the analysis of atom, respectively molecule movement. The basic idea is to iteratively integrate the equation of motion

$$\boldsymbol{F}_i(\{\boldsymbol{r}\}) = m_i \ddot{\boldsymbol{r}}_i \tag{2.11}$$

for each particle i, with mass m_i at position $\boldsymbol{r}_i$. The interactions between the particle and surrounding potentials result in the force $\boldsymbol{F}_i(\{\boldsymbol{r}\})$ acting on the particle. Hence we can write the acting force as the gradient of a position dependent interaction potential $U(\{\boldsymbol{r}\})$ as

$$\boldsymbol{F}_i(\{\boldsymbol{r}\}) = -\nabla_{\boldsymbol{r}_i} U(\{\boldsymbol{r}\}). \tag{2.12}$$

In a system of N independent particles this leads to N coupled differential equations of the form

$$\ddot{\boldsymbol{r}}_i = -\frac{1}{m_i} \cdot \nabla_{\boldsymbol{r}_i} U(\{\boldsymbol{r}\}), \tag{2.13}$$

for which there is no analytical solution if $N > 2$, but can be solved approximately with an iterative scheme.

2.3.2 Integrators

Integrators are algorithms for numerical integrations. In MD simulation, integrators can be used to integrate the equations of motion and yield the trajectories of atoms. In terms of MD simulations this requires the inclusion of thermodynamical behavior, which is done by modifying particle dynamics, i.e. their equations of motion. Therefore, an integrator must be chosen in accordance to the desired thermodynamical ensemble.

Microcanonical ensemble integrators must consider the conservation of energy. A symplectic integrator fulfills this requirement. The one which is used in this work is called Velocity Verlet algorithm. An integration step updates the position $\boldsymbol{r}$ and the velocity $\ddot{\boldsymbol{r}}$ of particle i at time t. Their new values at time $t + \Delta t$ can be calculated by

$$\boldsymbol{r}_i(t + \Delta t) = \boldsymbol{r}_i(t) + \dot{\boldsymbol{r}}_i(t)\Delta t + \frac{1}{2}\ddot{\boldsymbol{r}}_i(t)\Delta t^2 \tag{2.14}$$

$$\dot{\boldsymbol{r}}_i(t + \Delta t) = \dot{\boldsymbol{r}}_i(t) + \frac{1}{2}\left(\ddot{\boldsymbol{r}}_i(t) + \ddot{\boldsymbol{r}}_i(t + \Delta t)\right)\Delta t. \tag{2.15}$$

Canonical ensemble integrators are used for temperature control, e.g., when the system needs to be equilibrated at room temperature. Therefore, those integrators are called thermostats. In this work we use the Nosé-Hoover thermostat [26]. In terms of real variables one can write the Hamiltonian as

$$\mathcal{H} = \sum_{i=1}^{N} \frac{\boldsymbol{p}_i^2}{2m_i} + \mathcal{U}(\boldsymbol{r}^N) + \frac{\xi^2 Q}{2} + Lk_\mathrm{B}T \ln s, \tag{2.16}$$

where $\boldsymbol{p}_i$ denotes the momentum of a particle and m_i the mass. The degrees of freedom goes into L and k_B and T are the Boltzmann constant and the temperature. This is extended by an additional coordinate s, as well as a momentum p_s and an effective mass Q associated to it. The thermodynamic friction coefficient is denoted as $\xi = sp_\mathrm{s}Q$. Hence, the equations of motions can be denoted as follows:

$$\dot{\boldsymbol{r}}_i = \frac{\boldsymbol{p}_i}{m_i} \tag{2.17}$$

$$\dot{\boldsymbol{p}}_i = -\partial_{\boldsymbol{r}_i}\mathcal{U}(\boldsymbol{r}^N) - \xi \boldsymbol{p}_i \tag{2.18}$$

$$\dot{\xi} = \left(\sum_i \frac{p_i^2}{m_i} - Lk_\mathrm{B}T \right) \frac{1}{Q} \tag{2.19}$$

$$\frac{\dot{s}}{s} = \frac{\mathrm{d}\ln s}{\mathrm{d}t} = \xi. \tag{2.20}$$

2.3.3 Short range interaction

In this work we use the concept of short ranged particle interactions. Therefore, we restrict the number of interactions for a particle to only near surrounded particles. The basic idea is to have a cutoff distance, respectively cutoff radius r_c at which the interaction potential is assumed to be negligible. In figure 2.7 an illustration of the cutoff radius is shown, as well as a typical cell distribution in two dimensions. The particles (little dots) are distributed onto a grid of cells, namely MD cells. A particle can then only interact with particles within the same and eight neighboring MD cells as highlighted in the figure. In three dimensions there are 26 neighboring cells in total. For parallelization purposes the MD cells are distributed onto a super-lattice of CPU which is illustrated by different colors.

2.3.4 EAM potentials

We use Embedded Atom Method (EAM) potentials for our simulations to describe the interatomic interactions. In molecular dynamics they are commonly used for metals and metallic alloys and the model was first introduced by Daw and Baskes [27]. It uses a pair potential ϕ_{ij}, which describes the electrostatic core-core interactions and another

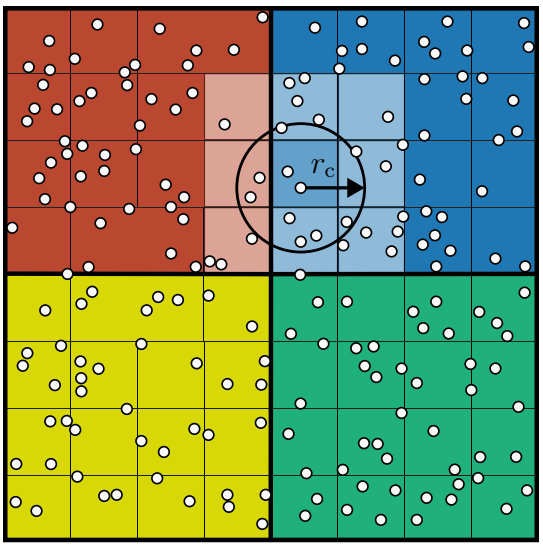

Figure 2.7: The sketch shows the basic concept of short range interaction in two dimensions. The chosen particle can only interact with other atoms within the range of the cutoff radius r_c. By introducing an MD cell grid, the interaction of this particle is limited to the nine highlighted cells.

term F_i which accounts for the energy increment when embedding an atom into the local electron density ρi. Hence, the total energy of the system can be written as

$$E_{\text{tot}} = \sum_i F_i(\rho_i) + \frac{1}{2}\sum_{i \neq j} \phi_{ij}(R_{ij}), \tag{2.21}$$

with the distance R_{ij} between atoms.

2.3.5 Implementation of laser irradiation

This section describes the basic idea of how laser interactions are implemented. We just want to present the basic idea of how the laser interaction is implemented. A detailed version of the derivation can be found in previous works though [9, 10].

Energy rescaling can be used to rescale the kinetic energy of the atoms with respect to the beam intensity. In general, this seems to be a straightforward approach, but it neglects not only the photon-electron interaction, but also thermalization through electron-electron interaction and the electron-phonon coupling. Since we use a much larger time scale in our simulations compared to the time scale of thermalization, a

localized increase of the kinetic energies is justified. The laser intensity according to which the kinetic energies should be rescaled is of the form

$$I(x,y,z) = (1-R)\cdot I_0 \cdot \exp\left(-\mu z\right) \cdot \exp\left(-\frac{(x-x_0)^2+(y-y_0)^2}{2\sigma^2}\right), \tag{2.22}$$

where I_0 denotes the maximum intensity, which is attenuated by the reflectance R as pointed out in section 2.2 and by the attenuation coefficient μ according to the Beer-Lambert law. The last term corresponds to the Gaussian shape of a laser beam with variance of σ^2 and a center at x_0, y_0. If we integrate the radial intensity, the maximum intensity can be expressed by the total laser power $P_{\text{tot}}/2\pi\sigma^2$. Because we need the change in kinetic energy for a discrete volume and time step we have to derive the intensity with respect to z and get

$$\frac{\mathrm{d}E}{\mathrm{d}V\,\mathrm{d}t} = (1-R)\cdot\frac{\mu P_{\text{tot}}}{2\pi\sigma^2}\cdot\exp\left(-\mu z\right)\cdot\exp\left(-\frac{(x-x_0)^2+(y-y_0)^2}{2\sigma^2}\right). \tag{2.23}$$

An extension to the absorption coefficient is needed in cases, where the absorption coefficient μ does not vary with z as in equation (2.23), e.g. for spherical surfaces. Because for light traveling through vacuum there is no absorption at all. This is the reason for the modification shown below. The basic idea is to perform an integral to get the absorption along z. The requirements for the modification are:

- only occupied cells should absorb,
- takes material dependent absorption into account,
- should work with load balancing (see section 2.4) and
- works regardless of parallelization.

Hence, we want a density and material dependent absorption coefficient. The requirement of parallelization is obvious, but the point of being used together with load balancing was the main reason for this modification and is also the reason for the chosen concept. The basic concept is to loop over all MD cells and calculate the absorptance of each cell correlated to the atoms in it and store the values in some kind of global array which is accessible for each CPU. To use it in equation 2.23 we have to sum up all absorptances from cells above.

2.4 Optimization methods

This section covers some common methods used for optimizing MD simulations in terms of computational efficiency. If we start with a basic system of N particles and do not consider anything but the atomic interactions, the computation effort scales with N^2.

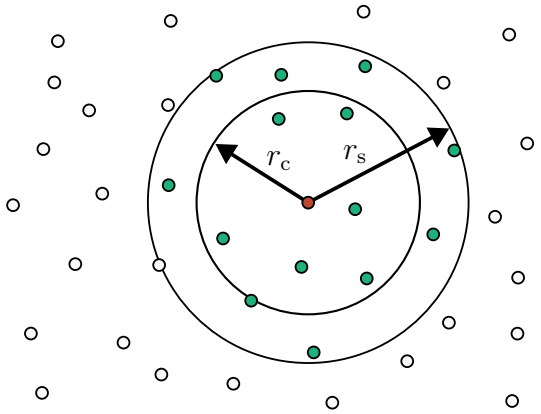

Figure 2.8: Sketch to visualize neighbor lists.

The short range interaction from section 2.3.3 limits the number of interactions for a particle to neighboring MD cells, leading the algorithm to scale with N. Therefore, this may also be attributed as an optimization technique. However, the concept of MD cells is an integral part of the simulation program used, whereas the methods we present in this section are optional.

Neighbor lists follow a similar approach as MD cells. Figure 2.8 shows a sketch that illustrates the concept. Each atom is attributed an environment by the cutoff radius r_c and a second radius r_s, which is the cutoff plus a certain margin. All particles within the range of r_s (green) are assigned as neighbors to the central particle (red) and stored in some kind of list. When calculating the particle's interactions, only the neighbors in its particular list need to be taken into account. The neighbor lists remain valid, as long as no particle move more than the margin $r_s - r_c$, otherwise they need to be recomputed. This approach can reduce the number of interacting particles and thus, the computation effort substantially. We can combine neighbor lists and the MD cell approach to improve the computation of neighbor lists, since this would scale with N^2 without MD cells.

Load balancing describes the process of distributing computational tasks in such a way that they are balanced in terms of parallelization and efficiency. In MD we can use load balancing for inhomogeneous samples, e.g. a single droplet in a rectangular box. There are different schemes of load balancing, but in this work we use adaptive load balancing, where needed. The adaptive load balancing scheme is illustrated in figure 2.9 for two dimension. The sketch shows how an unbalanced load is redistributed from a regular distribution on the left, to the balanced version on the right. Whereas moving the boundaries parallel to the simulation box, the adaptive load balancing scheme instead moves the corners of domains independently. The attraction of the corners is implemented by applying a force to them, which takes the number of particles into account. The acting force acts in the direction of high load and shifts the domain

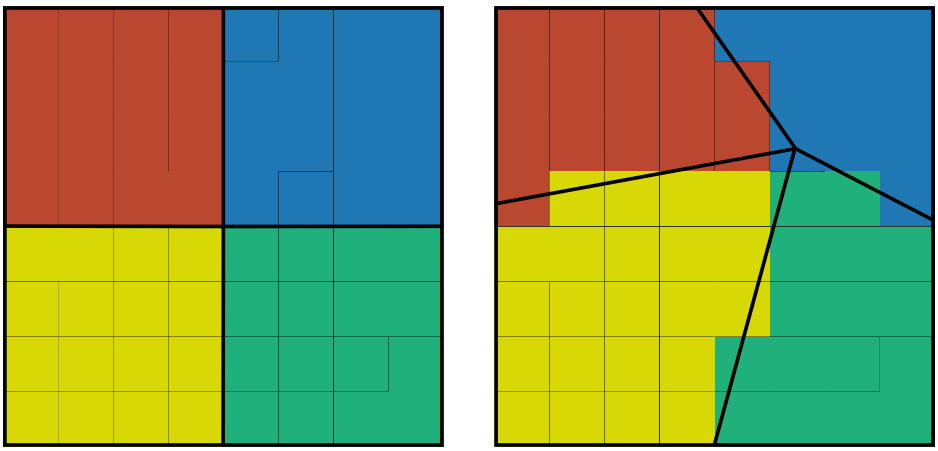

Figure 2.9: Sketch to visualize adaptive load-balancing for an inhomogeneous particle distribution. On the left side is an unbalanced load with regular MD cell to CPU distribution, whereas the domain corners on the right are attracted by the high load in the blue domain, resulting in a redistribution of MD cells.

corners accordingly. Therefore, domains of high load shrink and others grow. In figure 2.9 the highest load is within the blue domain, which results in it's shrinkage. However, there is already the MD cell grid to which the atoms belong to, that's why we reassign the MD cells instead of single particles.

Removing boundaries is less a kind of a common optimization method but the result of performance analysis compared with the knowledge of previous experiences. The problem is that a significant part of atoms can left the simulation box (e.g. for large laser irradiation). This goes along with a redistribution of atoms to CPU which could lead to a huge unbalanced load. The solution implemented in this work is to remove those atoms from the simulation by defining a certain boundary. However, this comes with the downside of unwanted interactions when removing an atom from an environment of interacting atoms (like it is the case for a blasted off melting droplet flying through such a boundary). To avoid such unwanted interactions, a cluster analysis (see section 3.3) for the removal of isolated particle groups can be implemented.

3 Methodology

In this chapter we discuss the methodological instruments that we use for the simulation and its evaluation. Section 3.1 introduces the used simulation program and delivers a basic knowledge of how to work with it. Afterwards, section 3.2 covers the process of preparing a sample to have it ready for an LPBF simulation. Finally, section 3.3 explains the analysis tools used for evaluation.

3.1 The used MD simulation program

For the simulations in this work we use our in-house MD simulation code *IMD (ITAP Molecular Dynamics)*, which is designed for large-scale simulation studies in materials sciences [28]. IMD is designed to be compiled manually by including only necessary part of the code for the desired simulation, which makes the binaries very small. However, if we want a binary to perform LPBF simulations, an appropriate compilation command would be

```
make clean && make imd_nve_mpi_slm_laser_eam_loadbalance_nbl
```

where the used options are separated by underscores.

The option `nve` is the desired thermodynamical ensemble, which activates the appropriate integrator explained in section 2.3.2. There are two parallelization modes available in IMD and we use the message passing library MPI, because we use short-range interactions as described in section 2.3.3. With the options `slm` and `laser` the necessary code part for LPBF gets included, which also involves the modifications pointed out in section 2.3.5. The option `eam` activates the usage of EAM potentials for atomic interactions as described in section 2.3.4. They are used in tabulated form as files. There is a potential set for the Ti-Al system available from Zope and Mishin [29] which was used for the simulations in this work. It has been developed by fitting to experimental as well as ab initio data. Finally the options `loadbalance` and `nlb` demand the code part for the optimization methods, explained in section 2.4

Now that there is a binary, we must define some necessary parameters for the simulation. This takes place in a separate parameter file. An appropriate content of such a file can be found in appendix A.2. The prepared simulation is then typically scheduled to some kind of batch system. The simulations for this work were carried out at the *HLRS (High-Performance Computing Center Stuttgart)*.

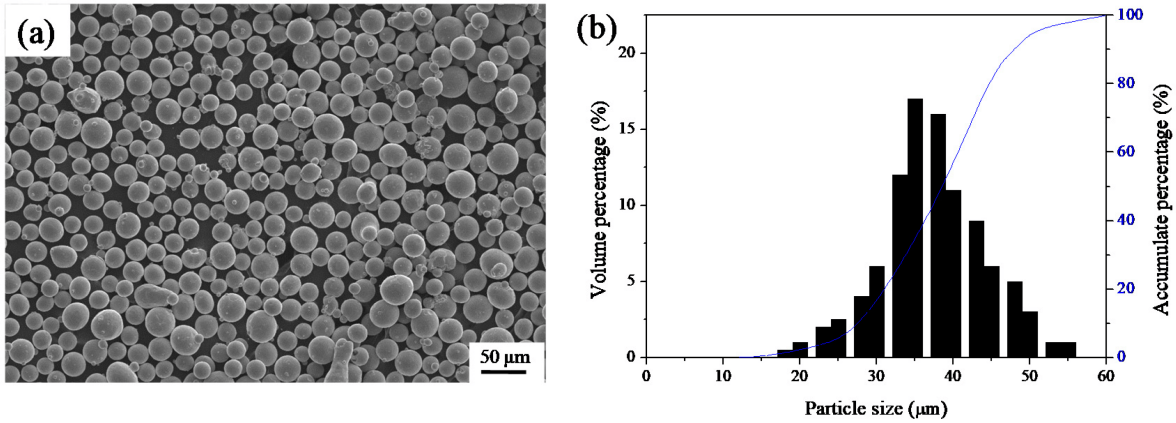

Figure 3.1: The powder morphology of Ti-6Al-4V on the left and the particle distribution on the right [30].

3.2 Preparing a sample

In this section we will go through the process of preparing a sample, ready to perform an LPBF simulation. When we talk about a sample it basically means a file which contains at least all necessary properties of each atom. To create such a configuration of atoms we first need to know how to design a proper sample within its environment. This is explained in section 3.2.1 and 3.2.2, where we look at how to choose an appropriate grain size and explain the need of a fixed atom layer. Afterwards we show how to create the desired atom configuration which takes place in section 3.2.3. To have the created configuration usable for the simulation, one need to equilibrate it at a desired temperature. Finally, section 3.2.4 covers the equilibration process.

3.2.1 Choosing an appropriate system size

In this section we want to deal with the task of choosing a sensible powder grain size. In principle we have to balance between a good representation of real grains and the limitations in computational expense. In figure 3.1 the morphology of a gas-atomized Ti-6Al-4V powder as well as its particle size distribution is shown. We can see that the powder grains are typically spherical and only few grains are shaped irregularly. Therefore, we limit our simulation samples to spherical powder grains.

The obtained particle sizes ranging from 15 µm to 58 µm [30] and from the corresponding particle distribution we take a mean size of about 35 µm, which can be assumed to be common. If we roughly estimate, there are about

$$N = \frac{6.022 \cdot 10^{23}\,\mathrm{mol}^{-1}}{74.848\,\mathrm{g\,mol}^{-1}} \cdot 4\,\mathrm{g\,cm}^{-3} \cdot \frac{4}{3}\pi \left(\frac{35\,\mu\mathrm{m}}{2}\right)^3 = 7.22 \cdot 10^{14} \tag{3.1}$$

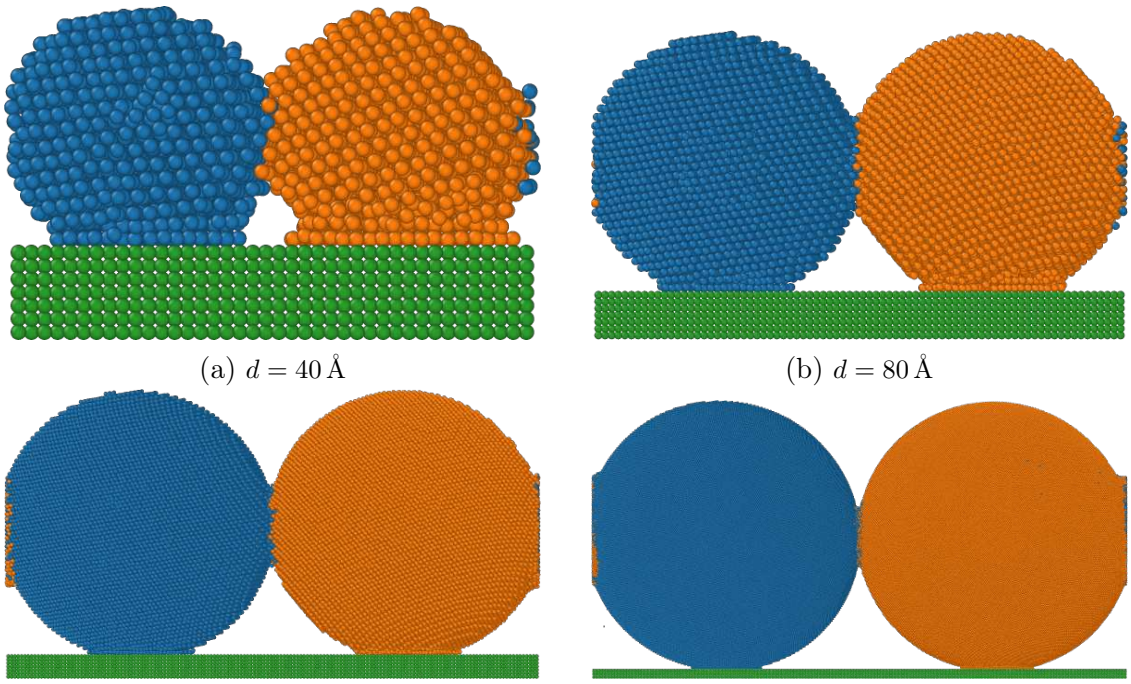

(a) $d = 40\,\text{Å}$ (b) $d = 80\,\text{Å}$

(c) $d = 160\,\text{Å}$ (d) $d = 400\,\text{Å}$

Figure 3.2: Comparison of spherical γ-TiAl grains with different diameter d, equilibrated on a fixed bottom layer. The bigger the grains, the better.

atoms in a single powder grain. In contrast to that, we usually deal with a few million atoms in our MD simulations. Although the degree of parallelization can be increased further, we are nonetheless limited in computational possibility and the manageability of large atom systems in terms of memory usage. Therefore, one has to choose a system size which stays manageable and makes sense in terms of the physical behavior.

In figure 3.2 we show a size comparison of a system with two γ-TiAl grains on a fixed γ-TiAl layer. The colors don't respect the atom type but separate the individual parts. For a diameter of $d = 40\,\text{Å}$ we observe the grains to be unusable due to their relative high surface interaction in comparison to their size. Especially the interaction with the substrate seems to be enlarged greatly, because the included gravity even supports the flattening. Hence, we have a non negligible cohesive attraction.

However, the larger we choose the spherical grains, the less we observe this side effect, even though the contact area increases. This fact is also observable if we calculate the ratio of the contact area in proportion to the whole sphere surface area. To simplify this task we just look on the two dimensional projection and calculate the ratio between the measured contact width to the calculated perimeter. These values are listed in table 3.1.

We combine all considerations and conclude that we need at least a diameter of $d = 80\,\text{Å}$ for the spherical grains, which corresponds to about 16500 atoms for the γ-TiAl

Table 3.1: Values for the contact width to perimeter ratio.

Diameter d [Å]	Contact width w [Å]	Perimeter p [Å]	w/p
40	27.83	125.66	0.22
80	38.34	251.33	0.15
160	62.47	502.65	0.12
200	103.94	1256.64	0.08

system. The bigger we choose our grains, the more accuracy we get. Computational manageability is the limiting factor here. The efficiency and manageability are experience values which have to be carried out. For this work we use either one large grain with diameter $d = 400\,\text{Å}$ or a set of multiple smaller grains with diameter $d = 160\,\text{Å}$.

3.2.2 The need of fixed atoms

In principle, we want to simulate an LPBF process. This involves to exert a certain amount of gravity on the grains so that they behave like real grains. Especially, we want the parts to behave as we would expect if they got melted or vaporized. Although we apply a gravitational force to the atoms, we have to increase it about several orders, due to the limited time scale of our simulations.

Now that we know that there is gravity in the system, we intuitively conclude that atoms will eventually fall out of the simulation box if there are no boundaries applied. To address this, reflective boundaries can be added to the bottom of the box. However, this is not integrated in IMD. Therefore, we include a thin layer of atoms at the bottom of the simulation box. Hence, this atom layer works as kind of a substrate surface. The gravity for those atoms can simply be turned off, so they do not move downwards by their own. But this is also not sufficient enough, as can be seen in figure 3.3a. The chosen bottom layer is too thin and the grain sinks in too much. Therefore, we restrict

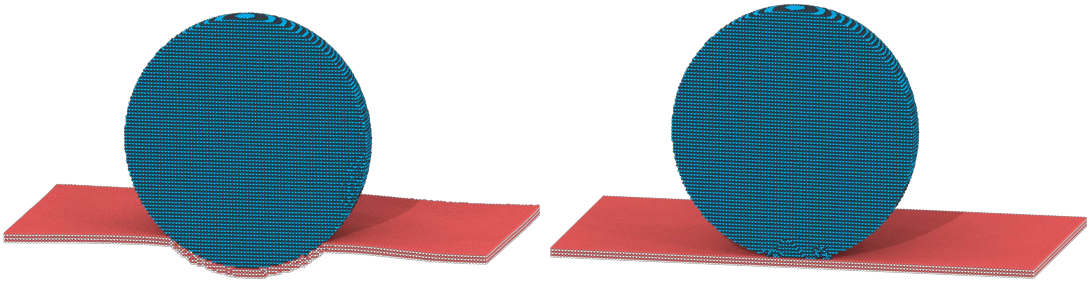

(a) Movable layer (b) Non-movable layer

Figure 3.3: A cut through a 300 Å grain on a movable or non-movable layer. The grain on the movable layer dips in too much, whereas the dynamics of the non-movable layer is neglected.

Table 3.2: Lattice structure, constants and atomic weights for the used materials [29, 31].

Material	Lattice structure	a_0 [Å]	c/a	Atomic weight m
Aluminium	fcc	4.05		26.981
Titanium	hcp	2.951	1.585	47.867
γ-TiAl	$L1_0$	3.998	1.047	

their movement by the usage of so-called virtual types, which is shown in figure 3.3b. Virtual types are an extend of the real types (Al and Ti) in such a way they have the same properties, but can be accessed more easily. The restriction in motion seem to be sufficient for our use case, but comes with the downside of neglecting the substrates dynamics and thus, with a loss of quality.

3.2.3 Creating atom configurations

In this section we explain how we create the desired atom configurations. In principle we have to deal with aluminium, titanium and the alloy γ-TiAl. The necessary properties to create a crystal lattice for these materials are listed in table 3.2. The lattice properties we use have been obtained by the developers of the EAM potential and in general there is good agreement with the experimental data [29].

Table 3.2 lists the used lattice structures fcc, hcp and $L1_0$. The first two are very common and therefore, need not be mentioned further. A sketch of the $L1_0$ structure is shown in figure 3.4. In principle it is an fcc lattice but with two different atom types arranged like shown in the sketch. Additionally, the lattice is not a cubic but tetragonal with a slightly bigger hight than the width of the square base.

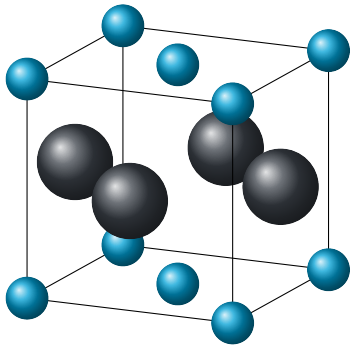

Figure 3.4: The $L1_0$ structure of γ-TiAl.

For the purpose of creating the desired atom configuration a simple program has been written. The main requirements for the development of this program were that

- it can create the desired lattice structures,

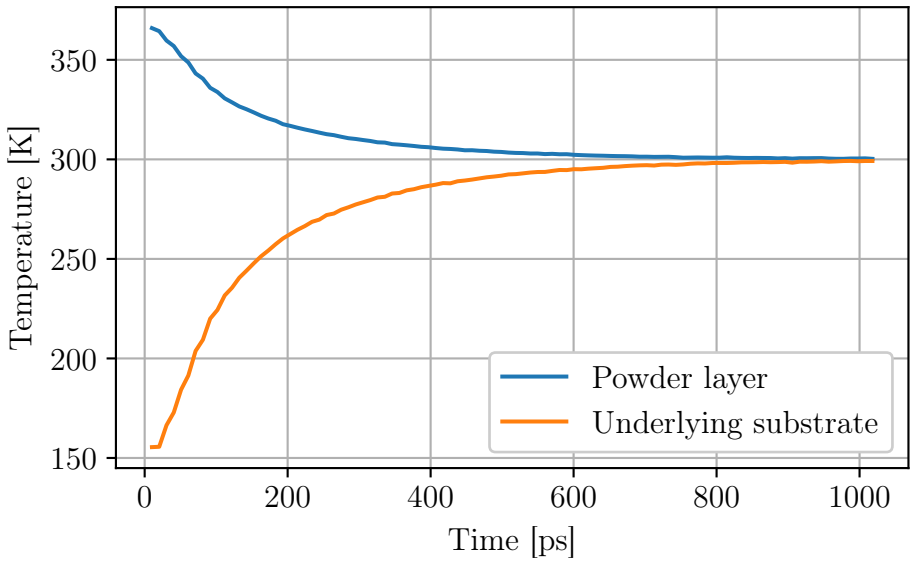

Figure 3.5: A typical temperature progression for an NVT simulation.

- it creates large configurations quite fast,
- it should have basic functionalities like cutting, shifting and rotating and
- it does not require multiple executions nor merging of multiple configurations.

To create an atom configuration, we pass the needed parameters as command-line arguments or parse them from a file. An example of a parameter file to create the atom configuration shown in figure 3.2d can be found in the appendix A.3.

3.2.4 Equilibration

Up until now we attributed just positions and masses to each atom. However, we want to have the configuration at room temperature. Therefore, they need to have a certain velocity. This is done as described in section 2.3.2 by using a thermostat. Figure 3.5 shows a typical progression we observe for this simulation. What is striking above all is that the temperatures of the powder layer and underlying substrate are separated for most of the time. Only towards the end the temperatures seem overlap. The temperature of the powder layer is the average of all powder grains. Therefore, some of them may start with a temperature below the heat bath temperature of 300 K, depending on their position in the simulation box. However, one can adjust the parameter τ_η to control the thermostat. It is a time constant which defines the time of a temperature oscillation and correlates with the effective mass Q from section 2.3.2.

The equilibrium process describes the fact that there is a minimal energy that each atom wants to reach and from a thermodynamic perspective will any undisturbed system eventually reach equilibrium. The process to get there is called equilibration. For our

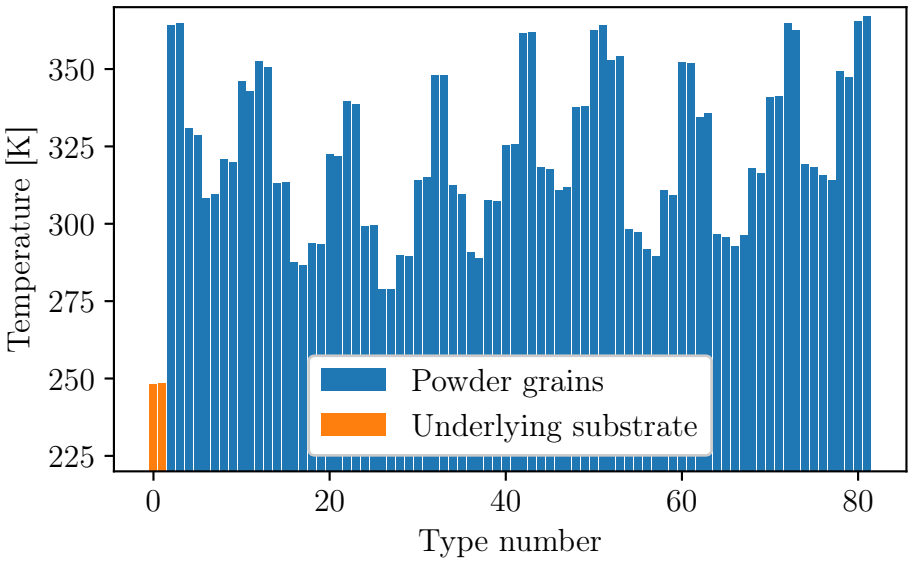

Figure 3.6: The temperature profile of a powder bed that is not yet equilibrated.

purposes, we speak of thermal equilibrium being achieved when there is no longer any noticeable change.

We calculate the temperature profile after an NVT simulation for the powder beds we will use in section 4.3. The temperatures are calculated for each virtual type individually and we remember ourselves that virtual types are just as real atom types, but can be addressed more easily. The calculated temperature profile is shown in figures 3.6 and 3.7. For example is the underlying substrate a γ-TiAl alloy and thus, consists of two (virtual) types. What we can take from figure 3.6 is a really inhomogeneous temperature profile along the different grains and substrate. The reason is that equilibrium is not reached yet and the temperatures will almost certainly change. This fact is further supported by the progression in figure 3.5.

In figure 3.6 we can see a single part of the system being overheated. The reason for that is a heat-up of just a few atoms. Thus, their velocities are increased drastically and they are far away from the simulation box. This behavior could also be observed within the temperature progression as shown in figure 3.5, but without averaging the temperatures. However, the total temperature of the system reached the desired temperature closely, because it's the average over all particle temperatures.

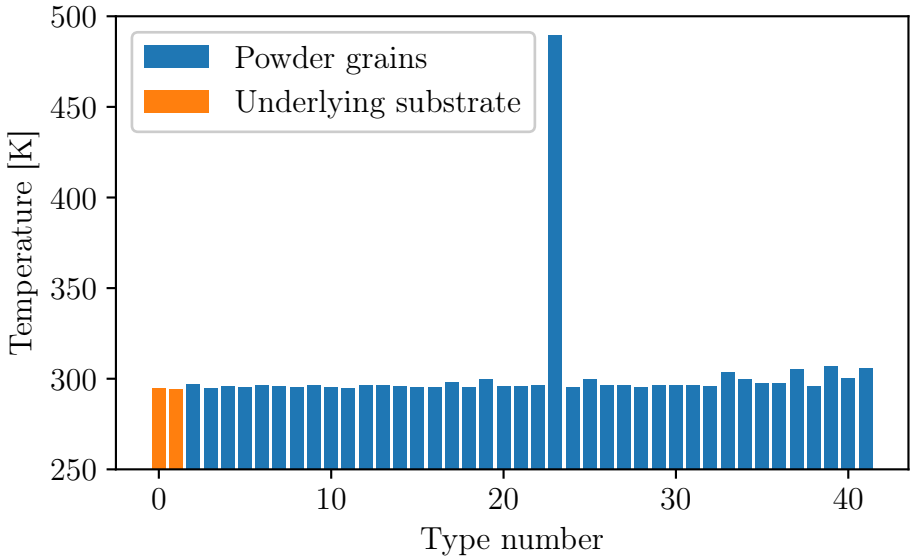

Figure 3.7: The temperature profile of a powder bed with a single grain being overheated.

3.3 Analysis tools

In this section we want to take a look at the analysis tools that have been used to inspect the simulations and evaluate the results. In principle, we use a mixture of existing tools together with self-written scripts.

Graphical visualization is the most common used tool to get quick insights from simulations. When we perform simulations with IMD, the produced data are typically stored in form of files that include calculated values like new atom positions. In order to evaluate this data, a graphical visualization is essential. The tool we use for this purpose is the Open Visualization Tool OVITO [32]. It has a graphical interface as well as a standalone Python package which can be used on devices without graphical user interface. With this tool we can get meaningful insights from our simulations, which includes the analysis of created atom configurations, as well as studying the material dynamics in form of animations.

Common Neighbor Analysis (CNA) is an algorithm which can be used to classify atoms in crystalline systems. That means we can differentiate if an atom belongs to a crystal lattice like fcc or not. In this work we use the CNA with a variable cutoff radius, which is implemented in OVITO and may also be called adaptive CNA.

For our analysis of molten fractions the CNA is our main criteria when we have to choose if a particle is assumed to be molten or not. However, atoms on surfaces doesn't have a complete neighborhood of atoms and therefore, do not belong to a crystal lattice within

this method. In order to calculate the molten fraction we subtract atoms which initially aren't assigned to a lattice structure.

We take a look at the basic concept of the CNA approach which is described in more detail in an article by Stukowski about its implementation [33]. The concept of the CNA is to get the neighbors of an atom within its cutoff radius r_c and calculate the triplet $(n_{\mathrm{cn}}, n_{\mathrm{b}}, n_{\mathrm{lcb}})$ for each of the N neighbor bonds of the central atom. A comparison of the calculated triplet with reference signatures can then be used to assign a structural type to the central atom. The meaning of those characteristic numbers are:

n_{cn}: The number of common neighbor atoms for a central atom and its bonded neighbor.

n_{b}: The number of total bonds between these common neighbors.

n_{lcb}: The number of bonds in the longest chain of connected common neighbors.

If we look for example on an hcp lattice we have $N = 12$ and six bonds are of type $(4, 2, 1)$ and the other six are of type $(4, 2, 2)$.

The basic idea of the CNA method is clear, but it is not well suited for a multi-phase system, because a variable cutoff radius is required for each atom then [33]. We call this approach *adaptive CNA*. Because this is the used method in this work we will simply refer to it as CNA from now on.

However, the $L1_0$ structure of γ-TiAl needs an extension which takes also the atom type into account. Although there already are extended versions to the common neighbor analysis for binary atomic system [34], we use the CNA of OVITO. Therefore, the γ-TiAl is assigned an fcc structure.

Cluster analysis is used to identify separated groups of particles. Those isolated particle groups are called clusters. A cutoff distance distinguishes if a certain particle connects to such a cluster or not. We can sort the size of the cluster in terms of number of particles it connects and use it, e.g., to identify the biggest cluster of the system. Another possibility for this analysis is to use if for the removing boundaries, mentioned earlier. However, we use the cluster analysis as a tool to inspect, rather than use it in the simulation itself.

4 Results and evaluation

This chapter covers the results and evaluation for the MD simulations of LPBF and contains two parts in general. The first one is the study on single powder grains, which is shown in section 4.1. For those results we use the version of IMD without the implemented modifications mentioned earlier. The second part is dedicated to a more demanding powder rather than single powder grains. This is explained in section 4.3 and uses the modifications of the absorption coefficient. In between both parts, section 4.2 shows a validation of the implemented modifications in order to justify its application.

4.1 Single powder grains

In this section the results for the study on single powder grains are presented. We will first take a look at powder grains with different configurations of binary material in section 4.1.1. Afterwards a laser scanning speed comparison is shown in section 4.1.2.

4.1.1 Coating material comparison

The basic idea is to compare the coated configurations with a γ-TiAl configuration. The used configurations are illustrated in figure 4.1. As mentioned, we use coated configurations with the first one being a titanium sphere, coated by an aluminium shell, the same vice-versa and the last one shows the homogeneous configuration of the γ-TiAl grain.

The grains are constructed with the methods and parameters pointed out in section 3.2. Basically, we create aluminium parts with an fcc lattice, titanium parts with an hcp

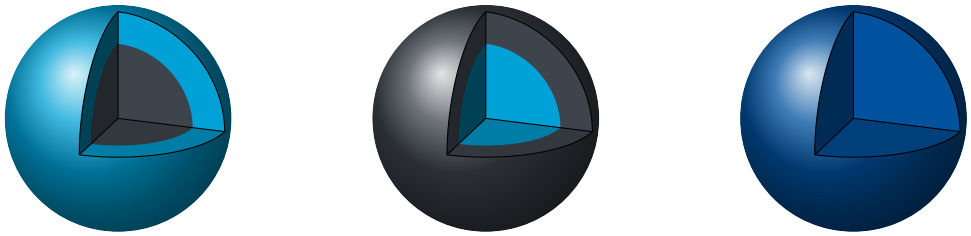

Ti core, Al shell | Al core, Ti shell | γ-TiAl sphere

Figure 4.1: Sketch to visualize the used configurations.

Table 4.1: Number of atoms for the different material configurations at $t = 0\,\text{ps}$.

Configuration	Ti atoms	Al atoms	Total
Ti core, Al shell	968 489	968 818	1 937 307
Al core, Ti shell	968 972	968 996	1 937 968
γ-TiAl sphere	1 032 735	1 032 832	2 065 567

lattice and γ-TiAl with the $L1_0$ structure. All spheres are created to have an outer diameter of 400 Å and a 50:50 ratio between titanium and aluminium. The number of atoms within these spheres are listed in table 4.1. Due to the different atom volumes of the crystal lattices, the number of atoms, as well as the diameter of the inner core varies. However, we include also a small layer of γ-TiAl on which we put the grains onto. The atoms of this substrate layer are fixed due to the reasons pointed out in section 3.2.2.

We perform laser melting simulations in terms of LPBF for all described configurations. For that we use a laser with velocity of 0.1 Å/10.18 fs and a power of 80 eV/10.18 fs. For the ease of use we neglect the reflectivity, because it is just a prefactor in our simulations. Hence, we have the opportunity to compare the results for the same injected energy.

The progression of the individual material configurations during the simulations is shown in figures 4.2, 4.3 and 4.4. According to these figures, the laser moves over the grains from left to right. We can see a lot of vaporization during the progression of these simulations. That's why we carried out a cluster analysis to clean up the images by hiding some vaporized atoms. However, the simulation progress is basically the same for each material configuration and we observe a burst and complete melting in all simulations, due to the chosen laser parameters.

Figure 4.2 shows the titanium core configuration coated with aluminium. We observe a bursting of the spherical shell at $t = 40\,\text{ps}$ and part of the titanium core is already vaporized. The chosen parameters, especially the laser velocity lead to a flower-like spread of the melted grain, visible at $t = 80\,\text{ps}$. Although the melted material has not yet fully settled, we observe a movement to the left and hence against laser movement. Additionally, we can see some smaller droplets, which have already fallen to the ground and are lying flat around the melted grain.

Figure 4.3 shows the aluminium core configuration, coated with titanium. As before we see a bursting of the shell at $t = 40\,\text{ps}$, which results in a lot of vaporization and the flower-like spread of the melted grain. The state at $t = 80\,\text{ps}$ shows an even more spread grain compared to the titanium core configuration. We also observe an almost complete settling of the leftover molt, although there are no small droplets on the ground yet. However, we can see some small droplets just before hitting the ground.

Figure 4.4 shows the γ-TiAl grain. In contrast to the coated grains we observe a total different progression in the long time limit. Although we can observe a similar bursting at $t = 40\,\text{ps}$ and have a flower-like spread at $t = 80\,\text{ps}$, the final simulation state shows a

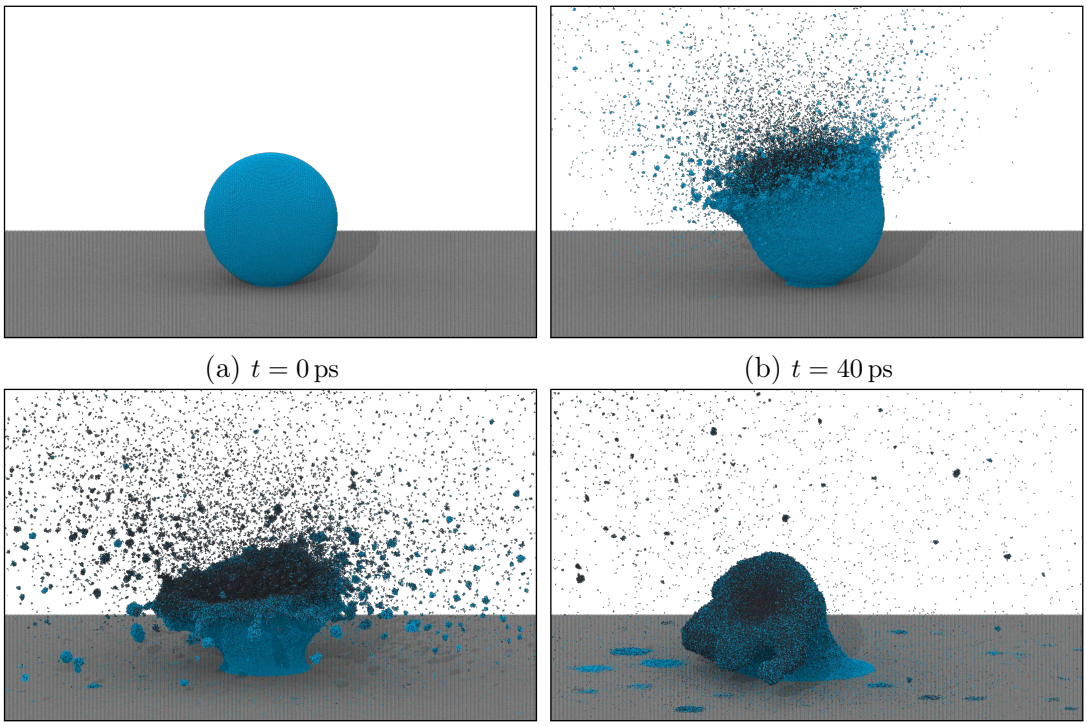

(a) $t = 0\,\mathrm{ps}$ (b) $t = 40\,\mathrm{ps}$

(c) $t = 80\,\mathrm{ps}$ (d) $t = 160\,\mathrm{ps}$

Figure 4.2: Simulation progress of the titanium core coated with an aluminium shell.

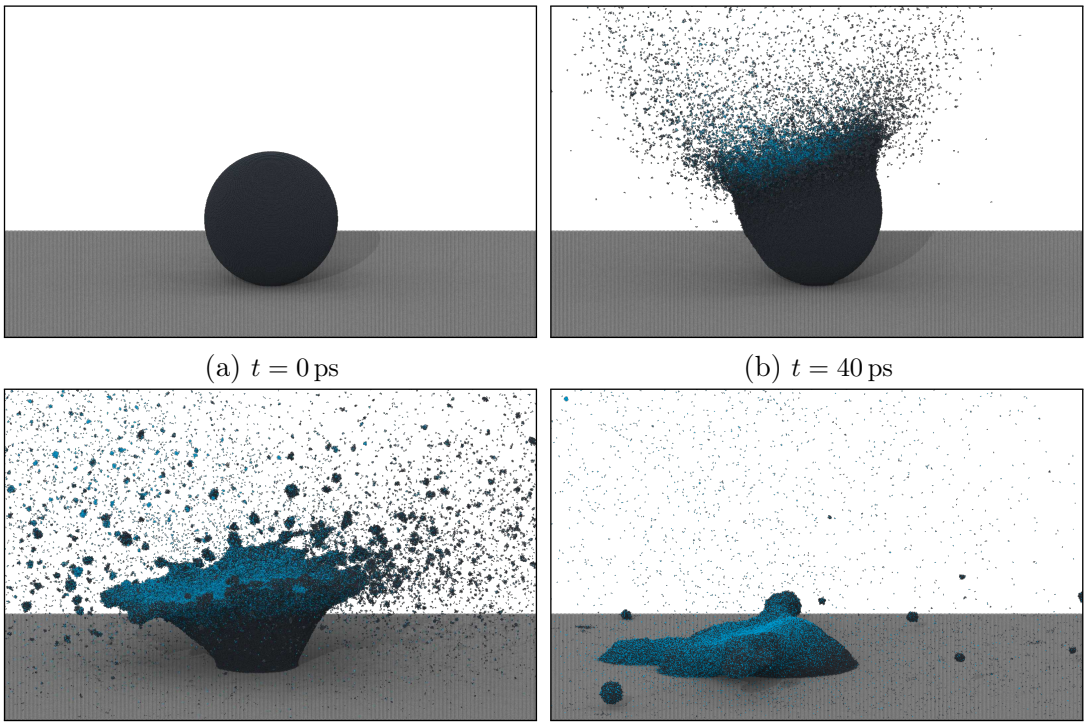

(a) $t = 0\,\mathrm{ps}$ (b) $t = 40\,\mathrm{ps}$

(c) $t = 80\,\mathrm{ps}$ (d) $t = 160\,\mathrm{ps}$

Figure 4.3: Simulation progress of the aluminium core coated with a titanium shell.

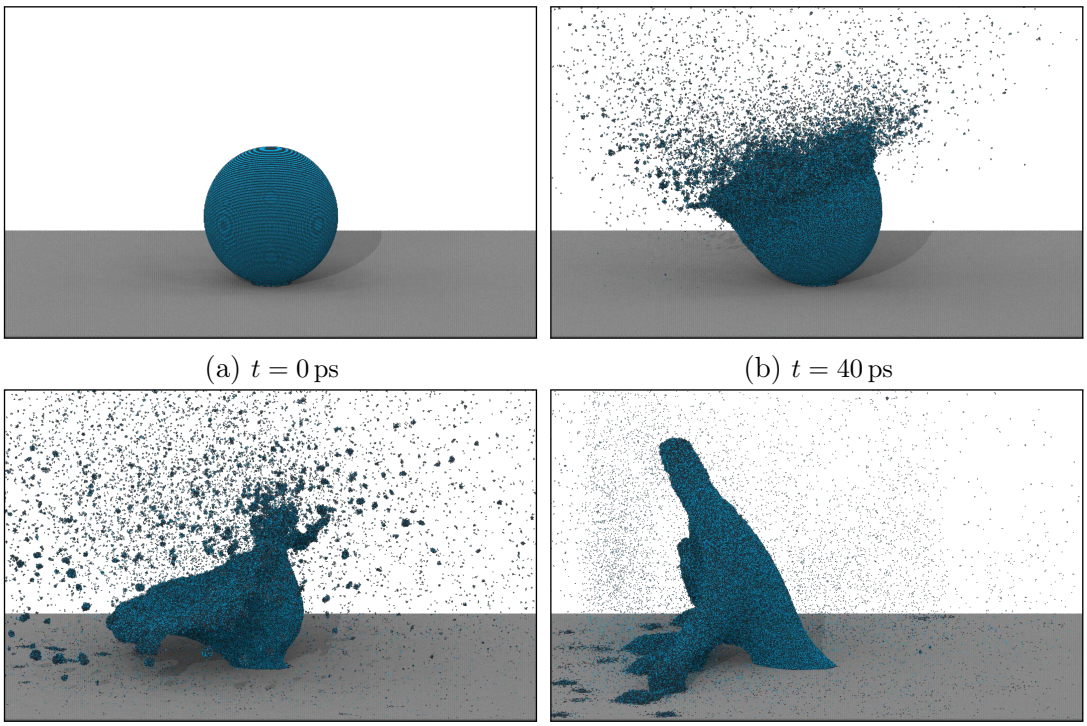

(a) $t = 0\,\mathrm{ps}$ (b) $t = 40\,\mathrm{ps}$

(c) $t = 80\,\mathrm{ps}$ (d) $t = 160\,\mathrm{ps}$

Figure 4.4: Simulation progress of the γ-TiAl grain.

tall upwards stretch of the melt. The reason is an increased movement against the laser, due to the chosen parameters. Even small differences and adjustments in simulation parameters can influence the material dynamics greatly.

We investigate the vaporization of both materials more closely and calculate the leftover proportion of aluminium atoms. We do so by carrying out a cluster analysis and only take atoms within the biggest cluster into account. The calculated values are listed in table 4.2. We obtain a decreasing aluminium proportion in the long time limit, independent of the material configuration. However, what strikes out is that the proportion of the configuration with an aluminium core rises first. This is in line with our expectations and observations from figure 4.4, because in the beginning, parts of the shell are vaporized first. Another main characteristic which can be taken from these values is that the final aluminium proportion varies with the distribution of aluminium. We obtain to have less aluminium evaporation the more aluminium is protected by surrounding titanium.

To complete this section we calculate the loss of aluminium during the simulations. The values are calculated in terms of the leftover melt, which is the biggest cluster, carried out by a cluster analysis. These losses of aluminium are listed in table 4.3. The slightest loss is obtained for the γ-TiAl configuration, which leads to the assumption that this configuration is the most stable in terms of total evaporation proportion.

Table 4.2: The proportion of aluminium atoms for the biggest cluster.

Configuration	Aluminium proportion [%] at $t =$			
	0 ps	40 ps	80 ps	160 ps
Ti core, Al shell	50.0	46.7	44.8	42.8
Al core, Ti shell	50.0	51.1	50.3	49.3
γ-TiAl sphere	50.0	49.8	48.5	47.2

Table 4.3: The loss of aluminium in terms of the biggest cluster.

Configuration	Loss of aluminium [%] at $t =$			
	0 ps	40 ps	80 ps	160 ps
Ti core, Al shell	0.0	16.3	38.0	44.5
Al core, Ti shell	0.0	10.6	34.0	40.4
γ-TiAl sphere	0.0	9.6	28.4	34.6

4.1.2 Laser speed comparison

In this section we investigate the influence of the laser velocity qualitatively. Therefore, we vary the laser velocity but keep the power constant. We expect to have a lower energy density for higher velocities. The confirmation of this assumption can be seen in figure 4.5. For the simulations shown in this figure we use the γ-TiAl configuration. We look at the samples from the left, this means looking in the direction of laser movement. For $v = 0.1\,\text{Å}/10.18\,\text{fs}$ we see the flower-like spread of molten material as mentioned earlier in section 4.1.1. An increase of the velocity to $v = 0.3\,\text{Å}/10.18\,\text{fs}$ leads to a weakening of this spreading and results in several fountain-like splashes. The grain does not melt completely and remains partly solid. For the hightest chosen velocity we obtain an almost half melted grain and the molten material splashes, forming a single tall fountain, which will eventually come off in the form of a drop.

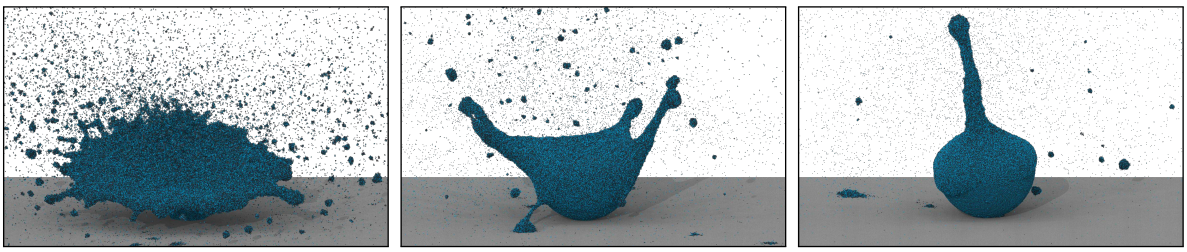

(a) $v = 0.1\,\text{Å}/10.18\,\text{fs}$ (b) $v = 0.3\,\text{Å}/10.18\,\text{fs}$ (c) $v = 0.5\,\text{Å}/10.18\,\text{fs}$

Figure 4.5: Simulation state after 80 ps for different laser velocities. The view is along direction of laser movement. With increasing velocity, the melting decreases and the molten splashes form single fountains.

4.2 Validation of implemented modifications

Referring to section 2.3.5 modifications have been implemented to better depict the material dynamics. This includes the integration of density dependency as well as material type dependency for the absorption coefficient. For the results in section 4.1 we used the old implementation, without this modification, but we will make usage of the modification from now on, starting with the comparison of both implementations. The aim of this section is to have a meaningful validation of the implemented modifications.

We prepare a sample which is shown in figure 4.6 and let the laser scan the surface from left to right across the step. According to equation 2.23 the injected laser energy depends on a fixed hight z. We thus, expect the injected energy to fall on a lower level when the laser reaches the lower step. In contrast to that, the new implementation should remain constant when crossing this step. This expectation is confirmed and shown in figure 4.7. We can see an increase of the injected energy in the beginning when the laser reaches the sample and also the characteristic decreasing when the laser leaves the sample. This comes from the Gaussian profile of the laser and can be obtained for both implementations. However, as we expected there is a change when crossing the step and the injected energy of the old implementation decreases about a third and apart from small fluctuations the injected energy of the new implementation remain constant when crossing the step.

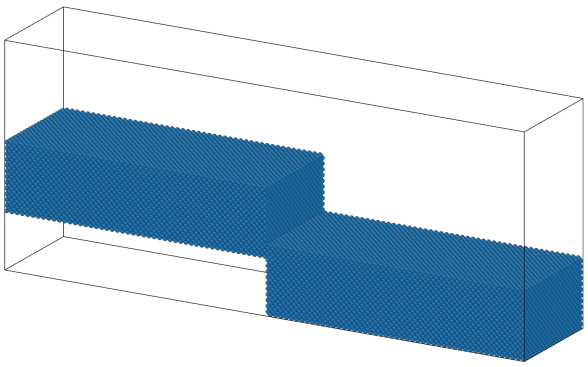

Figure 4.6: Aluminium atom configuration in a step shape.

One can also notice a small gap between the curves along the upper step. This may has its origin in the fact that there is no absorption attributed to any atom in the highest surface MD-cells and thus they collect more energy. Also the laser offset in the old implementation was set slightly above the surface, therefore also the outermost atoms receive less energy.

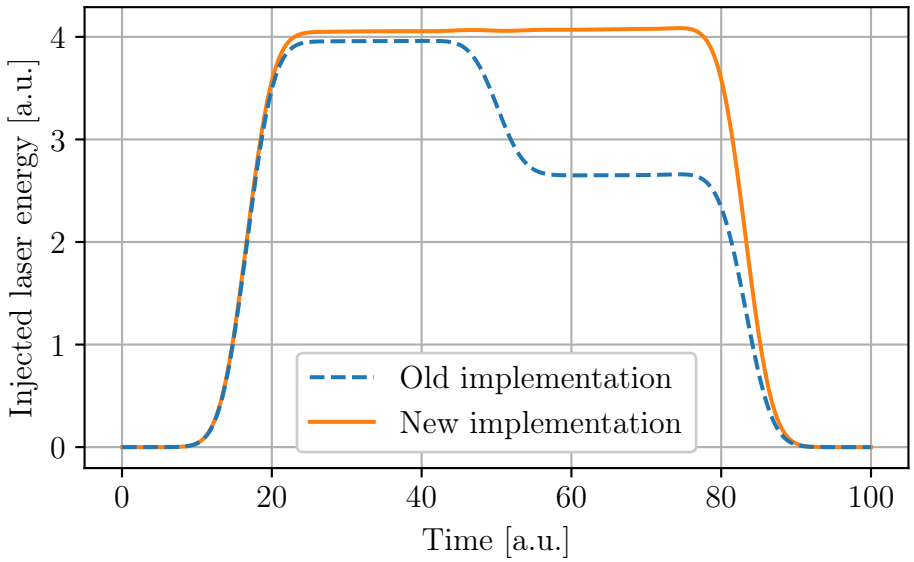

Figure 4.7: Comparison of injected laser energies for old and new implementation of the laser interaction. When scanning with the laser across a step shaped sample, the injected energy of the old implementation decreases, whereas the injected energy of the new implementation remains constant.

4.3 Towards real LPBF

The previous results show single powder grains on a fixed substrate surface and approved the general functionality of our LPBF simulations. However, if one would like to simulate more realistic LPBF a new approach with different requirements has to be chosen. This new approach and its results are presented in this section. At first, section 4.3.1 covers the requirements and how to construct samples. Afterwards, section 4.3.2 presents the used simulation parameters and introduces the used notation. Finally, sections 4.3.3 and 4.3.4 cover simulation results for LPBF of different powder beds.

4.3.1 A more demanding powder bed

When looking at a single sphere on a fixed layer we neglect some important aspects without which we cannot get insights into interesting parts of the LPBF process. The most obvious is that we need to put more grains into the simulations. But this in fact also comes with the downside of increasing the number of particles and therefore, increases computational costs. We thus need to choose a grain size which stays manageable to deal with and also reasonable regarding to the problems pointed out in section 3.2.1.

The aim is to create a minimal, yet simplistic powder bed. The chosen configuration is shown in figure 4.8. It consists of 40 powder grains in total. The underlying requirements were to have a multi layered powder bed. Thus, a minimum of two layers is

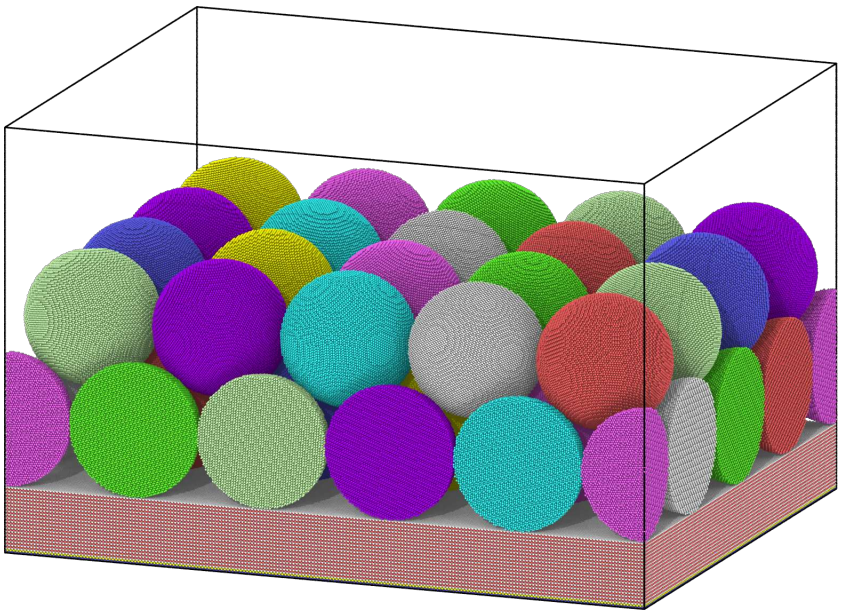

Figure 4.8: A more realistic powder bed configuration which fulfills more demanding requirements. The configuration consists of 40 powder grains, wrapped at periodic boundaries and rotated at random. A tiny layer of fixed atoms is placed beneath the substrate layer. Although they repeat, the colors do not represent anything but the individuality of each grain.

necessary. Due to the proportion of the laser beam we then need at least also two rows in the direction perpendicular to the laser scanning direction. We extend this about one row on each side to include the possibility for heat conduction towards the outside. Hence, we include the possibility to observe spacial melting transition and study the laser melt trace. However, since the laser velocity is very high compared to the size of the powder bed, we want to put most powder grains along the laser scanning direction which is why a number of five rows was chosen there.

To complete the requirements for the sample we replace the fixed substrate surface from previous simulations by a layer of γ-TiAl in the size of the grains radii and stick again a layer of fixed atoms beneath. Hence, the possibility for heat conduction into the underlying substrate, respectively the possibility to apply a cooling to the molten powder is given. Hereby also the dynamics of the substrate is taken into account though it is weakened by the fixed layer beneath.

As can be seen in figure 4.8, all powder grains have the same size, because this is the easiest and fastest way to create the atomic configuration. Otherwise, the powder grains have to be created and equilibrated in a way that they end up lying in a realistic manner, which is not trivial as they interact greatly between their surfaces. The grains in the chosen configuration though use a simple grid orientation where the layers are translated against each other and upper grains are placed on the sink which is formed by four underlying grains. Also they wrap at periodic boundaries in x and y direction

which can be seen by the corner grain on the lower layer, as it is the same for all four corners. In z-direction there are no periodic boundaries applied, because they would force atoms to stay in the simulation box and strong vaporization would then lead to wrong interaction. At least every grain is rotated at random to avoid side effects of using a single lattice orientation.

4.3.2 Simulation parameters and notation

This section covers the necessary parameters for the simulations. It treats also the notation, which is used for subsequent evaluation.

After equilibrating our samples at 300 K, a series of laser simulations is performed. The used simulation parameters are listed in table 4.4. All values are kept constant instead of the laser power. For the reflectance, the value of titanium is used, as there could no values been found for the optical properties of γ-TiAl. This seems to be an ugly workaround but up until now the reflectance is just a prefactor for the laser intensity calculation and doesn't matter much here. Thus, the total laser power is given as P_{peak} which takes the reflectance into account. A second note applies to the absorption coefficients. Although the ratio between both values are kept constant, they are scaled to half. However, this allows us to get a result where we have the substrate's surface partially melted.

Table 4.4: Parameters for the laser fusion simulations with demanding powder beds.

Name	μ(Ti) $[10^{-2}\,\text{Å}^{-1}]$	μ(Al) $[10^{-2}\,\text{Å}^{-1}]$	R [1]	v [Å/10.18 fs]	FHWM [Å]	P_{peak} [eV/10.18 fs]
P_{500}	0.471 87	1.1808	0.615 11	1.0	320	500
P_{1500}	0.471 87	1.1808	0.615 11	1.0	320	1500
P_{2500}	0.471 87	1.1808	0.615 11	1.0	320	2500
P_{3500}	0.471 87	1.1808	0.615 11	1.0	320	3500
P_{4500}	0.471 87	1.1808	0.615 11	1.0	320	4500
P_{5500}	0.471 87	1.1808	0.615 11	1.0	320	5500

For the notation regarding the assignment of powder grains we us a basic graphical approach. Hence, we have the opportunity to easily recognize which values belongs to which grains. Therefore, we take the sample showed in figure 4.8 and rotate it such that we look at the face side. The look from this side is schematically shown in figure 4.9. Since there are periodic boundaries in x and y direction applied to the simulation box, the half grains on the lower outside connect to each other and form a full row. The laser is moving into the drawing plane along the plane of symmetry. In the figure two grains are marked by fill them out in black. Hence, the notation ◗●○●◖ would belong to the lower grain rows which lay in between the center and outer rows and combines ten grains in total. Analogously, we define upper rows along the plane of symmetry by either ○●●○ for the two center rows or ●○○● for the two outer rows. Both combinations

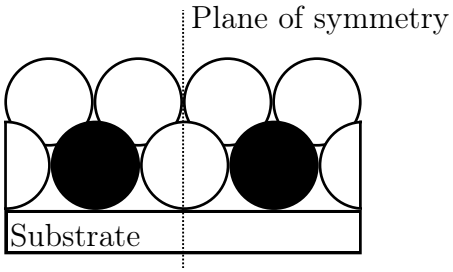

Figure 4.9: Sketch to illustrate the notation used.

contain also ten grains. Only the lower center row ◗○●○◖ and the lower outer row ◗○○○◖ combine just five powder grains each.

4.3.3 LPBF of γ-TiAl powder

This section shows the results for a simulation series performed with γ-TiAl powder grains. For the simulation series we use a powder bed constructed as described in section 4.3.1 which is shown in figure 4.10. As beforehand we use the colorization for better differentiation between individual powder grains. For the configuration we use again the lattice structure $L1_0$ of γ-TiAl. The spheres have a diameter of 160 Å and each one consists of about 128 000. Combined with the substrate which has 2 400 000 and the same lattice structure there are more than 7 560 000 atoms in the simulation.

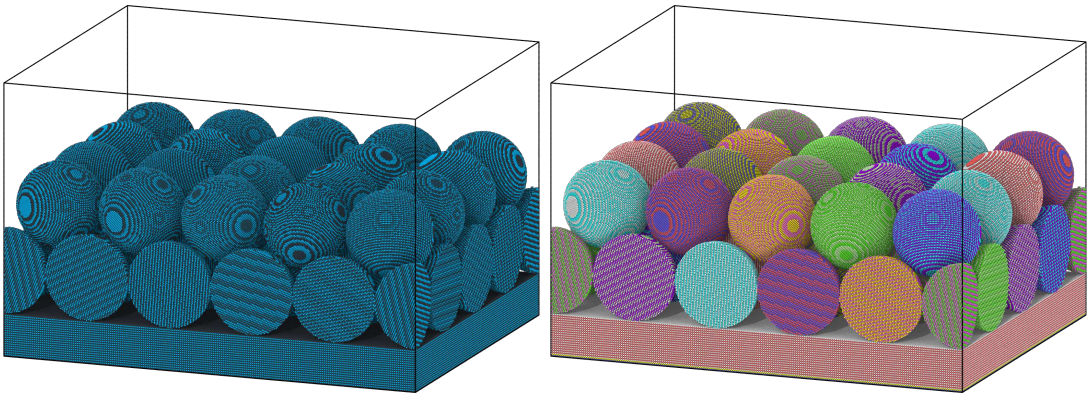

Figure 4.10: The atom configuration of a demanding γ-TiAl powder bed. On the left side titanium in anthracite and aluminium in blue. On the right the same configuration but colorized for better differentiation.

Final states

At first, we take a look at the final simulation states of our sample to make some qualitative statements. Those simulation states are shown with different view angles in figures 4.11, 4.12 and 4.13. Figure 4.11 shows a perspective view of the complete sample,

whereas the other views show only half part of the sample, because they were cut in half to see along the center of the sample which is the most interesting part. One must also keep in mind that the figures show the final simulation state after 200 ps, whereas the interaction of the laser takes place within just the first 17 ps. Hence, the material has time to settle down after it got lifted upwards due to the laser interaction.

In figures 4.11, 4.13 and 4.12 we see that the laser moved across the sample and leaves a melted trace along its movement, but only if the infused energy was high enough to reach this threshold. Qualitatively this threshold has been exceeded for simulations P_{3500}, P_{4500} and P_{5500}. A melting of row ◗○●○◖ up to the substrate, first takes place with P_{4500}, but only near to the center. A full melting of this row is only reached in P_{5500}, where even a complete fill up of empty spaces can be observed.

When looking at the substrate, and especially at figure 4.12 we recognize that even the substrate's surface gets partially melted with an increase of the laser power. Although this melting is mostly near to the center along the laser scanning direction, it's nonetheless a reasonable point to verify the quality of the simulation. This is because a good fusion of powder on top of the substrate requires melting of the substrate's surface.

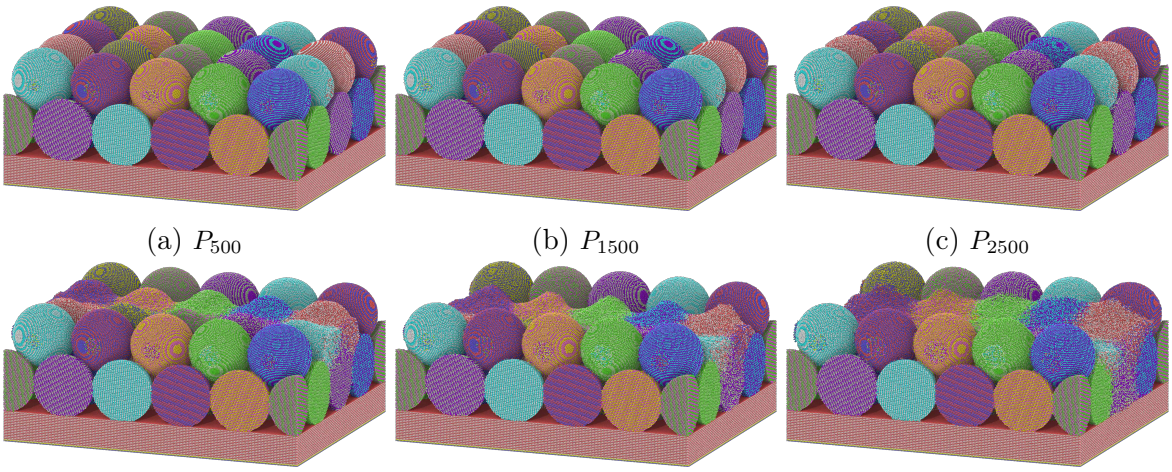

(a) P_{500} (b) P_{1500} (c) P_{2500}

(d) P_{3500} (e) P_{4500} (f) P_{5500}

Figure 4.11: Perspective views at $t = 200$ ps for the power series of γ-TiAl.

Melting mode

Previous simulations showed great vaporization when performing the laser melting simulations. However, although it was observed in previous simulation runs, there was no manifesting of vaporization in this case. The number of atoms which flew out of the simulation box are listed in table 4.5 together with the difference in the total temperature of the system. In fact, those values for vaporization are negligible and regarding to section 2.1.2 the threshold for a vapor cavity is not reached yet. Thus, the chosen parameters resembles the conduction mode, which is favorable for our simulations.

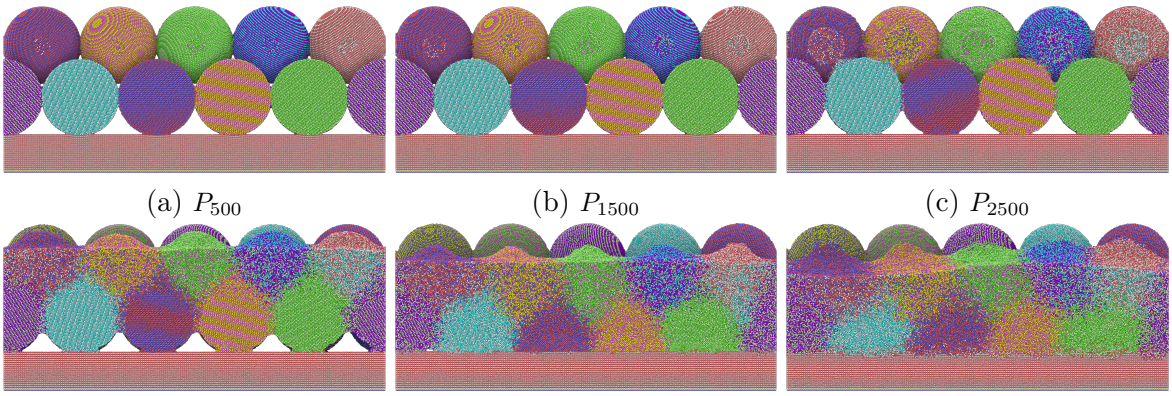

(a) P_{500} (b) P_{1500} (c) P_{2500}

(d) P_{3500} (e) P_{4500} (f) P_{5500}

Figure 4.12: Cutted front views at $t = 200\,\text{ps}$ for the power series of γ-TiAl.

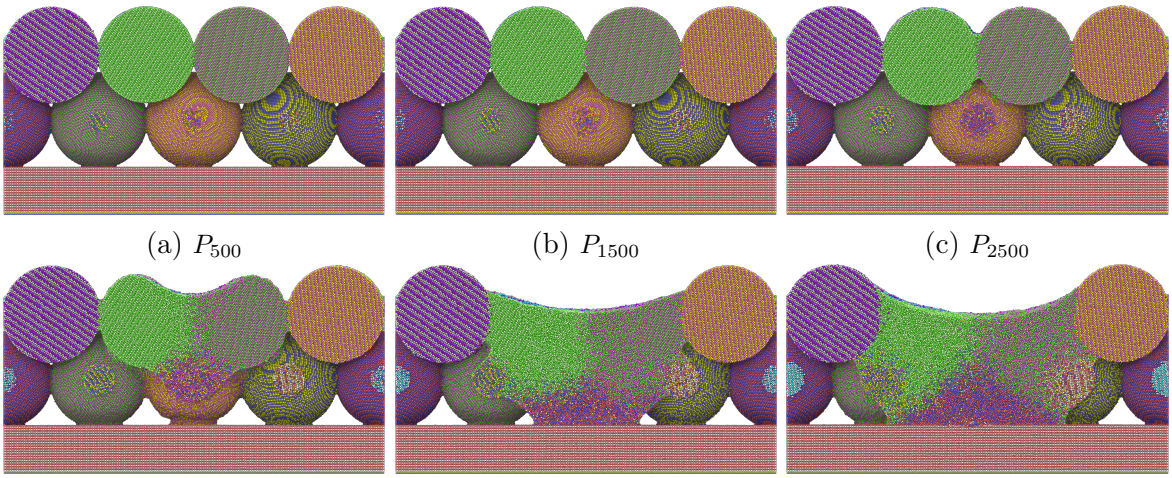

(a) P_{500} (b) P_{1500} (c) P_{2500}

(d) P_{3500} (e) P_{4500} (f) P_{5500}

Figure 4.13: Cutted left side views at $t = 200\,\text{ps}$ for the power series of γ-TiAl.

Table 4.5: Atom and temperature differences for the power series of γ-TiAl.

Simulation	Δ#Ti	Δ#Al	ΔT_{tot}[K]
P_{500}	0	2	118
P_{1500}	0	3	347
P_{2500}	0	0	566
P_{3500}	0	0	738
P_{4500}	0	1	884
P_{5500}	0	1	1053

Temperature profile

We extend our investigation and want to take a deeper look into the temperatures, because they give us not only information regarding melting and vaporization, but also about the heat conduction within the sample. The temperature profiles can be seen in figure 4.14. The pattern of the temperature progression is the same for all simulations. It starts at a minimum value and quickly reaches a higher value. After the energy injection stopped, heat conduction leads to a common temperature progression towards a constant level. Although the pattern is consistent in all simulations, it should be noted that the scaling of the temperature axis varies. Therefore, the individual simulations differ greatly in total temperatures recorded.

The trend of the curves is indeed almost the same though, no matter which laser power was chosen. Grain rows near the symmetry plain gain the most energy, hence they heat up the most. However, most interesting is the behavior after the laser interaction stopped, which results in a peak temperature for the two most hightest curves. There, the temperature of those rows start to decrease, whereas rows which are further on the outside heat up towards the end of the simulation. Hence, we observe heat conduction. The grains in the rows ◗○○○◖ seem to stay mostly constant though. However, if we look closer into these grains we find also a temperature gradient there. They may not change their temperature because they work as a conductor and already are near to the final temperature, which other grains will reach after some time too.

Molten fraction

To analyze the simulation series in more detail we finally take a look at the molten fraction during the simulation. This calculation was done by performing a CNA and exclude those atoms which initially aren't assigned to any local structural environment, as they likely sit on a surface and therefore do not contribute correctly to the molten fraction. The results of this analysis are shown in figure 4.15.

$\underline{P_{500}}$: In the corresponding graph only the mean values are depicted. This is because the molten fraction is less than 0.3 %. Therefore, the fluctuation in this range is relatively high and would lead to a great overlap of curves. The figure shows that there are some points where the molting fraction of ◗○○○◖ is less than zero, which is indeed not possible, but comes from the chosen normalization by neglecting initial atoms being not assigned to a local structural environment. The general arrangement of the individual curves is in fact plausible as the rows ○●●○ and ◗○●○◖ can collect the most energy, because they are aligned closest to the beam spot centrum.

$\underline{P_{1500}}$: The molten fraction for the grain rows ○●●○ and ◗○●○◖ collect the most energy again and thus their molten fraction increases the most. The peak is at the time where the laser leaves the sample and no more energy is injected. After the energy injection stopped, the melted part seem to recrystallize and therefore the molten fraction

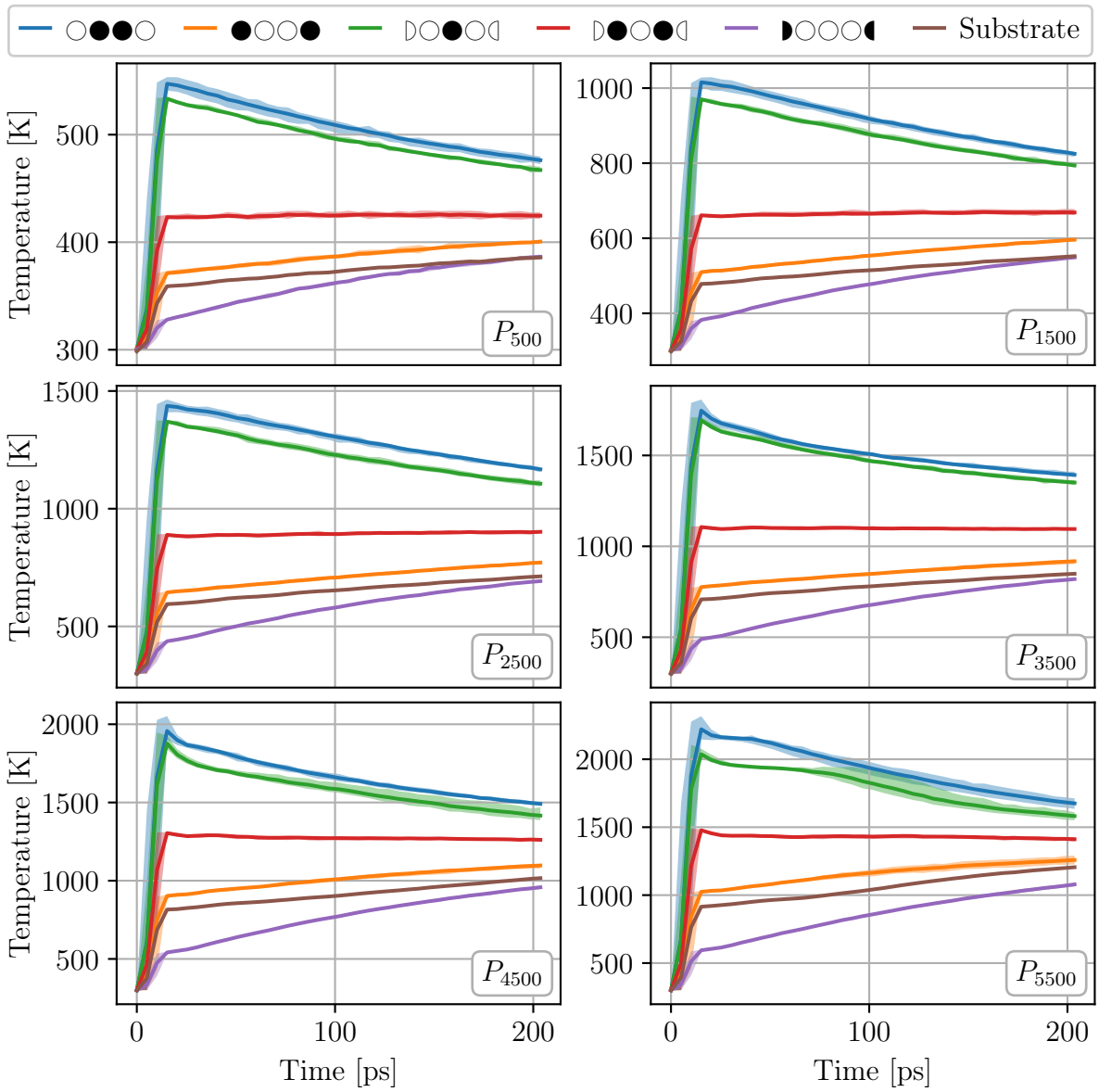

Figure 4.14: Temperature profile for the power series of γ-TiAl.

decreases again. Other rows and especially the substrate seems to doesn't gain enough energy and stay mostly solid.

P_{2500}: The molten fraction increases again so that the green and blue rows have their peaks between 30 % to 40 %. After energy injection stopped, these grain rows start to recrystallize again as beforehand. However, this is the first time a noticeable fraction of the substrate starts to melt. But one also have to take into account that the substrate's area is large compared to the grain diameter and melting of the substrate mostly takes place near the symmetry plane along the laser scanning direction. An increase of its molten fraction is therefore not directly comparable to the grain ones, although it could

give good information on melting quality.

$\underline{P_{3500}}$: The increase of the laser power causes a change in the recrystallization behavior as it is now a bit weakened. This could be explained by the lack of solid material. Thus, molten material has no good starting point for recrystallization, as the atoms can not find a structure to settle. The molten fraction of the grains in the row ◗●○●◖ also increased a lot but stay almost constant an no recrystallization is evident.

$\underline{P_{4500}}$: The most gainful grain rows almost melt completely and also extend the melting process even after the energy injection stopped. The other grain rows also got more melted and for the so far least gainful rows as well as for the substrate an increasing molten fraction is noticeable towards the end of the simulation. The start is approximately around 50 ps and in fact, lays past the stop of energy injection. Hence this must be caused from heat conduction. An effect from the grain dynamics due to the laser interaction could also play a role here.

$\underline{P_{5500}}$ The simulation with the most highest used laser power shows a completely melting of the rows ○●●○ and ◗○●○◖ . After the grains of these rows got melted they stay melted until the end of the simulation and no recrystallization is evident. Also an increase of the heat conduction towards the outside of the sample is noticeable and the molten fraction of the substrate reaches almost 25 % towards the end of the simulation.

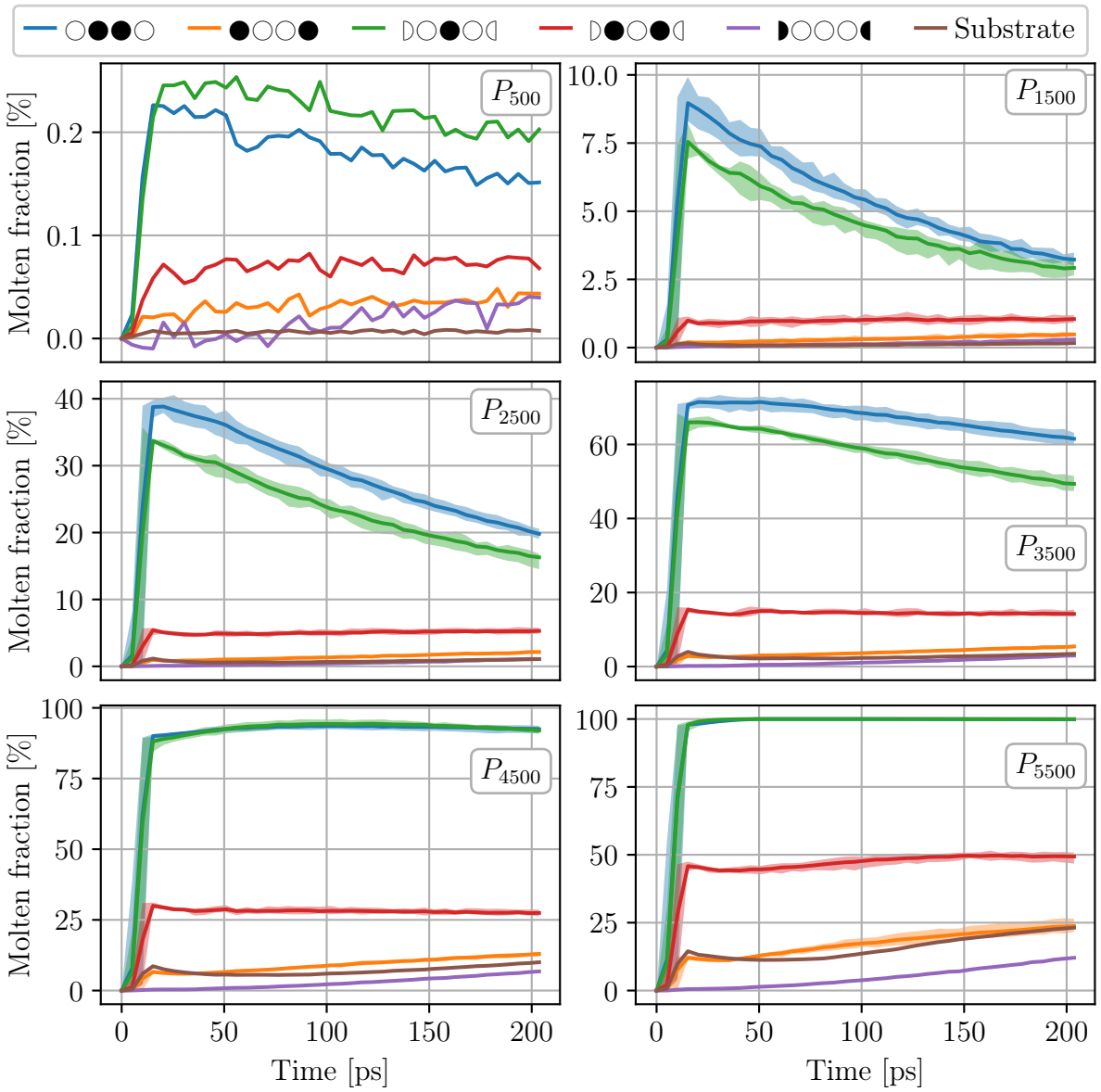

Figure 4.15: The molten fraction analysis for the power series of γ-TiAl.

4.3.4 LPBF of mixed Ti-Al powder

This section shows the results for a simulation series performed with a mixed powder of titanium and aluminium grains. Up until now, the implementation of the laser interaction uses a single reflectance not matter of the material. For our configuration, depicted in figure 4.16 this means that aluminium grains gain more energy as they normally would, because their reflectance in the simulation is chosen to low. However, we use the same simulation parameters as for the γ-TiAl powder series, which is listed in section 4.3.2. Thus, we can discuss the differences later on.

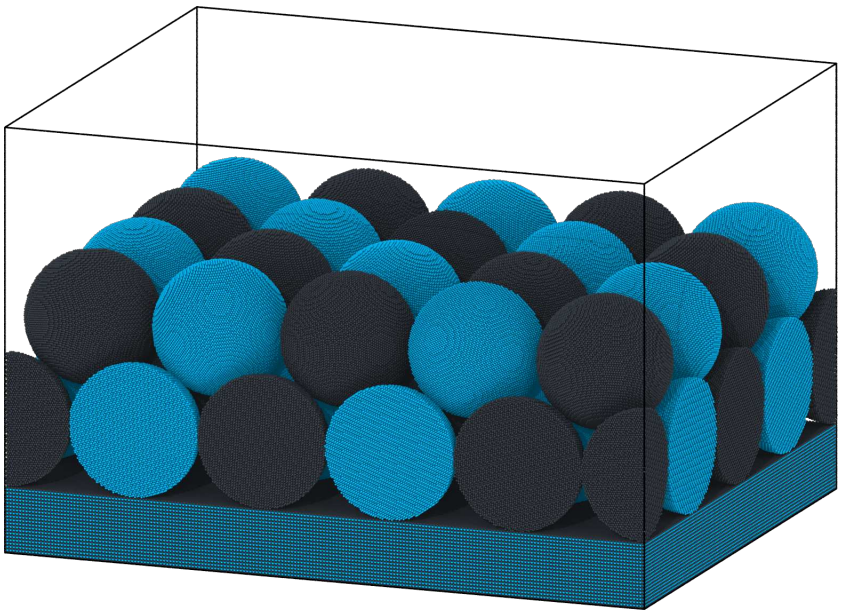

Figure 4.16: The atom configuration for the mixed powder bed with alternating grain types. Titanium is depicted in anthracite, aluminum in blue.

The sample is created by placing alternately a titanium and an aluminium grain along the direction with the greatest expansion. Due to the chosen dimension of the configuration grid, a real alternating pattern cannot be achieved and hence some nearest neighbors are of the same type. Although it was useful for previous considerations a more colorized version of the sample is not preferred here but can be found in appendix A.1.

There are about 7 400 000 atoms in the simulation. The titanium grains use an hcp lattice structure and each grain contains about 121 000. Aluminium grains are constructed with an fcc lattice and hence there are about 129 000 aluminium atoms in one aluminium powder grain. As beforehand we use a γ-TiAl alloy substrate which consists of about 2 400 000 atoms.

Final states

We first take a look at the final simulation states after 200 ps again, which are shown in figures 4.17, 4.18 and 4.19 using different viewing angels and cut in half as before. One can see that melting of aluminium is preferred, whereas titanium grains seem to melt only for high laser power. In fact, this difference can clearly be seen in figure 4.18c, where the aluminium melted mostly completely, but titanium grains remain solid. To remind again, there is a single reflectance applied, no matter of the atom type.

In contrast to the γ-TiAl powder bed, we observe for the largest laser power a complete melting of all aluminium grains. But not only the aluminium grains melted completely, it seems that also the amount of molten titanium grains is larger compared to the same grains of the γ-TiAl powder bed.

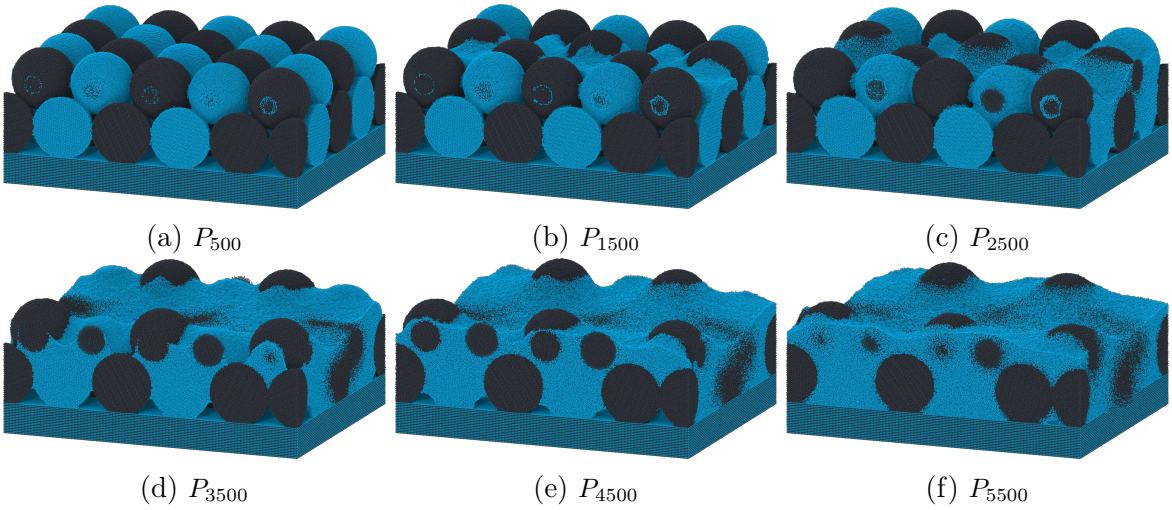

(a) P_{500} (b) P_{1500} (c) P_{2500}

(d) P_{3500} (e) P_{4500} (f) P_{5500}

Figure 4.17: Perspective views at $t = 200\,\text{ps}$ for the power series of mixed powder.

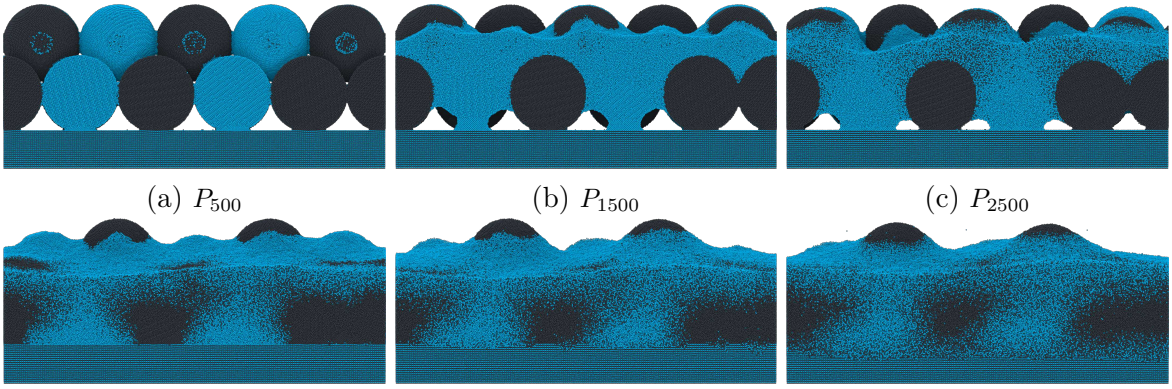

(a) P_{500} (b) P_{1500} (c) P_{2500}

(d) P_{3500} (e) P_{4500} (f) P_{5500}

Figure 4.18: Cutted front views at $t = 200\,\text{ps}$ for the power series of mixed powder.

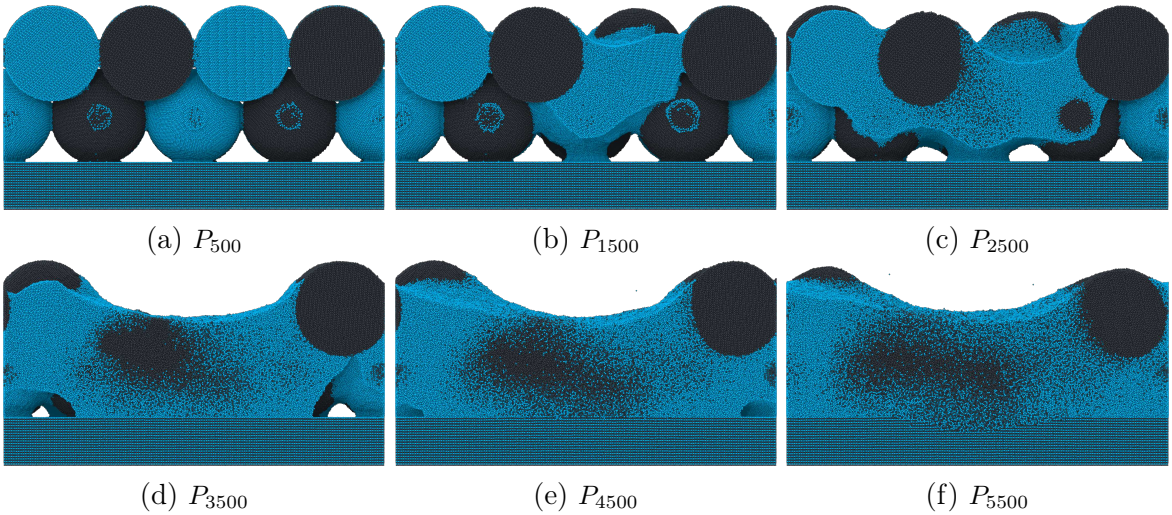

(a) P_{500} (b) P_{1500} (c) P_{2500}

(d) P_{3500} (e) P_{4500} (f) P_{5500}

Figure 4.19: Cutted left side views at $t = 200\,\text{ps}$ for the power series of mixed powder.

Interesting is the melt behavior of the substrate which can be observed greatly in figure 4.18. The melting depth in this cutting plane along the center increases with an increase of the laser power. The final result in P_{5500} seems very promising, because the substrate melted almost half from top. Also, the mixing of titanium and aluminium in this area seems qualitatively good enough for building up a valid alloy structure. In fact, the total atom mixing along these cutting plane seems to increase from 4.18d to 4.18f.

Melting mode

Due to the high melting observation of aluminium, we intuitively would think that there is a lot of vaporization going on there. In fact, the number of evaporated aluminium atoms which left the simulation box to the top is higher compared to the γ-TiAl powder bed. As long as the laser power is not increased further, the amount of vaporized aluminium also appears to be negligible. We therefore can again argue to be in conduction mode. The differences in atom number due to exiting the simulation box at the top are listed in table 4.6 together with the difference in the total temperature of the system.

Table 4.6: Atom and temperature differences for the power series of mixed powder.

Simulation	Δ#Ti	Δ#Al	ΔT_{tot}[K]
P_{500}	0	0	117
P_{1500}	0	0	350
P_{2500}	0	0	588
P_{3500}	0	6	854
P_{4500}	0	142	1106
P_{5500}	0	1004	1346

Temperature profile

The temperature profile of the mixed powder bed is shown in figure 4.20. When we look at those results, we first notice that the symmetry is broken, because we need now also a distinction between aluminium and titanium to combine different data sets into a single curve. The distinction between the atom types does in fact not restore full symmetry but is sufficient for our considerations. Hence, there are ten individual row combinations plus the substrate.

As expected, aluminium always gets its peak temperature above the corresponding titanium grains. However, an interesting finding is that no peak temperature is observed in conjunction with tatanium. Instead of cooling down, they heat up even after the energy injection has stopped. This means there is heat conduction between aluminium and titanium grains withing same rows. Finally, we observe that everything strives to a total temperature balance for long times.

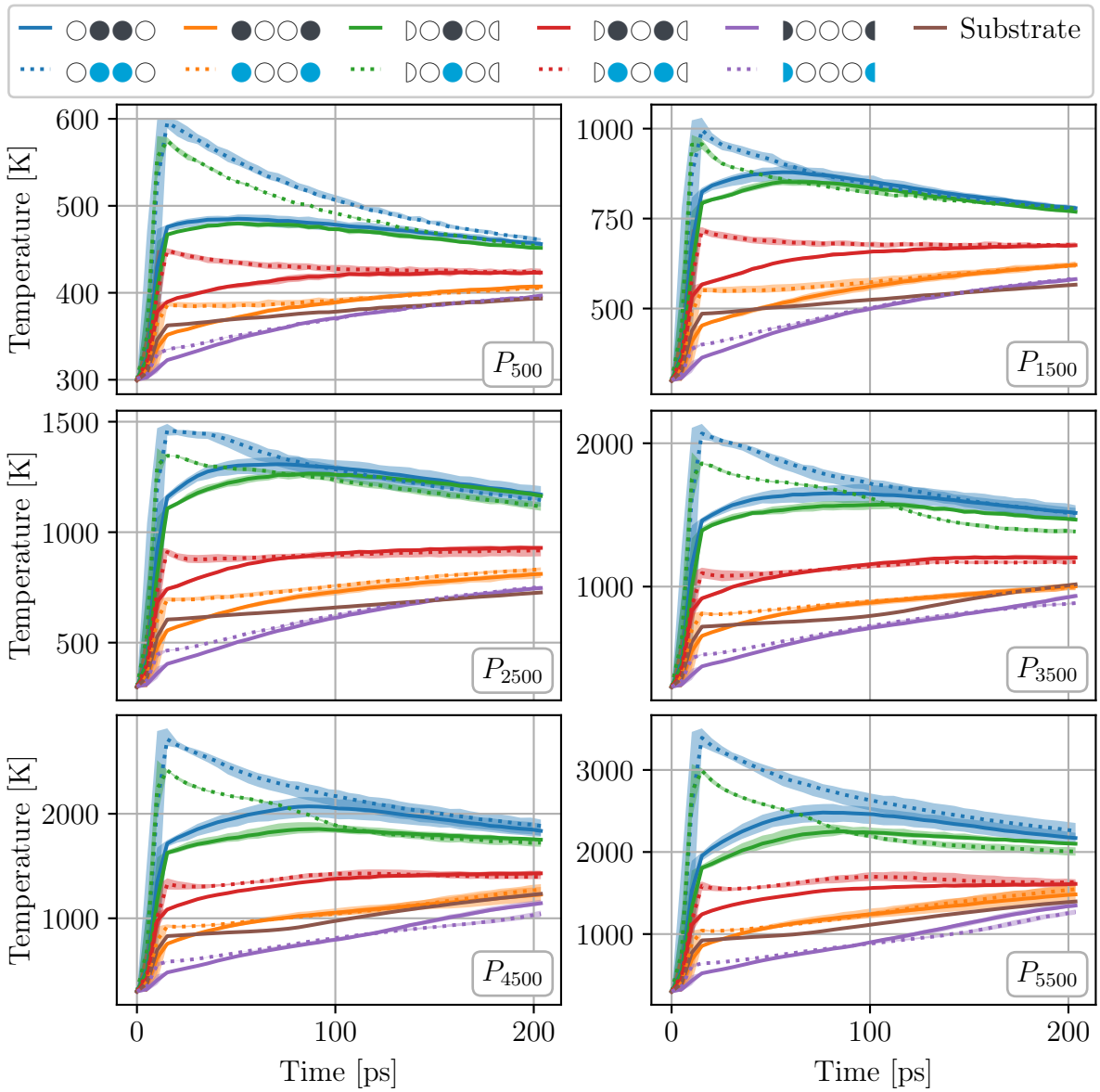

Figure 4.20: Temperature profile for the power series of mixed powder.

Molten fraction

We calculate the molten fraction by a CNA as before. The result for this analysis is shown in figure 4.21.

$\underline{P_{500}}$: Noticeable melting only takes place for the aluminium grains within the rows ○●●○ and ◗○●○◖ . They reach about 10 % molten fraction at their peak. After the laser left the sample and the energy injection stopped, recrystallization takes place and the molten fraction decreases to about 3 % towards the end of the simulation. Other rows in which a small melting can be observed also belong to aluminium grains.

$\underline{P_{1500}}$: Most melting can be observed within the aluminium grains near the centrum of the beam spot. They reached the threshold for molten fraction where the recrystallization is weakened.

$\underline{P_{2500}}$: The aluminium grains in the blue and green rows reached whole melting and stay melted till the end. The interesting part belongs to the other row though. While the titanium rows ○●●○ and ◗○●○◖ start to melt and recrystallizes towards the end, the melting of not fully molten aluminium grains increases constantly till the end of the simulation. They therefore gain energy through heat conduction.

$\underline{P_{3500}}$: Molten fraction of ●○○● almost reaches 100 % directly after the laser left the sample, but only reaches full melting after some time. Titanium grains rows ◗○●○◖ almost reaches full melting state and ○●●○ partially does. The trend of aluminium which is located further out is the same and the melting increases constantly towards the end, but with a higher rate as before. Also some portion of the substrate was melted too.

$\underline{P_{4500}}$: The most grains are molten completely at the end of the simulation. Only the substrate and titanium grains within the outer rows remain partially solid. Due to the excess energy, the substrate continue to melt.

$\underline{P_{5500}}$: The power of the laser was enough to melt all aluminium grains, but most outer titanium grains remain solid partially. The molten fraction of ●○○● is fluctuating greatly, because the number of grains differs as can be seen in figure 4.16. For the used laser power, the substrate almost reached 50 % molten fraction.

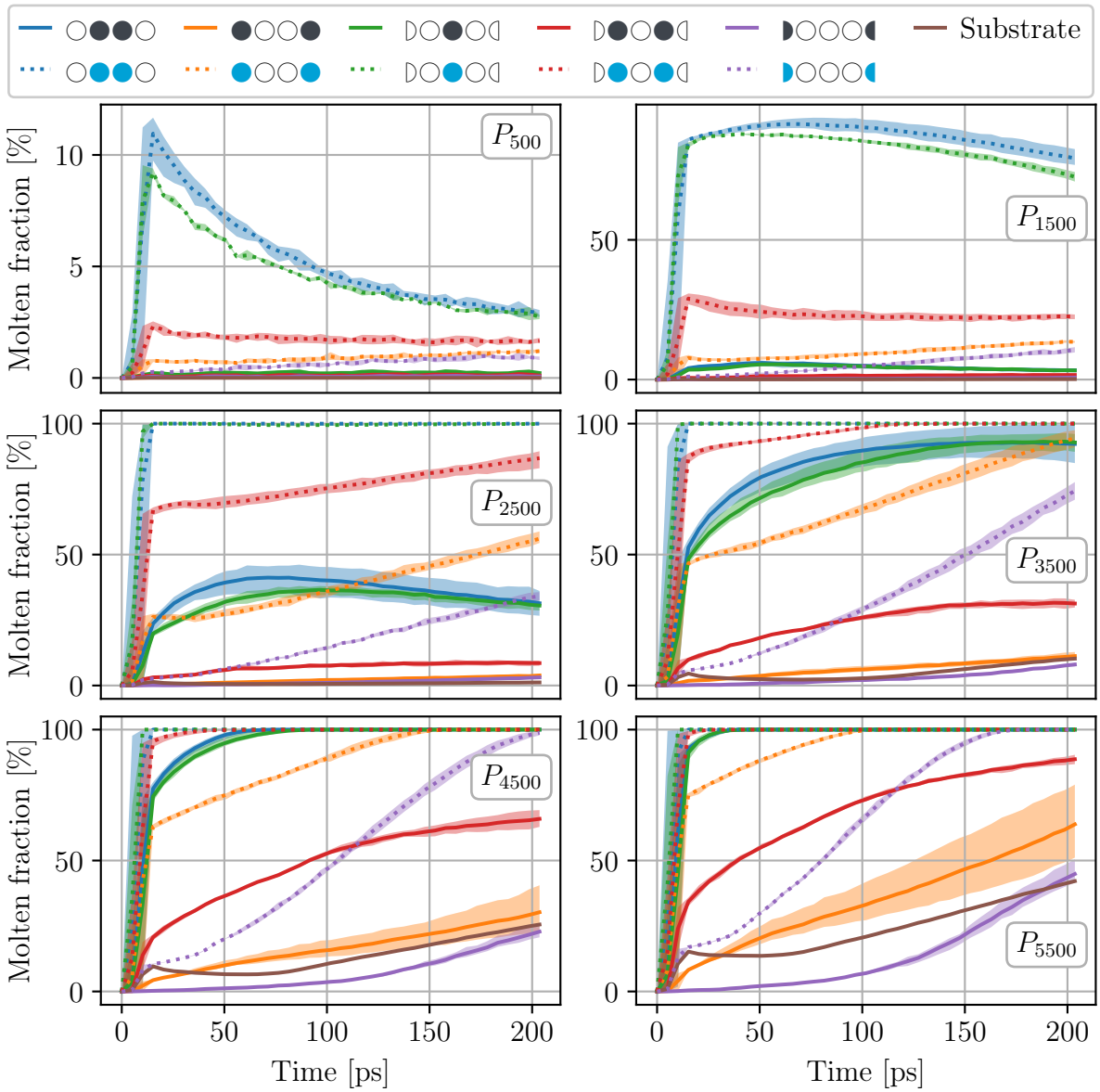

Figure 4.21: The molten fraction analysis for the power series of mixed powder.

4.3.5 Observable defects

We focus again on the results of the γ-TiAl powder of section 4.3.3. In principle one could say that we had lack of fusion in five out of six times, which agrees to the molten fraction we just calculated. However, when we look at figure 4.12e, we notice a small porosity one would likely overlook. Figure 4.22 shows this tiny pore in more detail. Despite it is not surrounded by material in each direction it's nevertheless an irregular cavity we don't expect here and hence, call it a pore. We can see that the pore is located between two grains. From the CNA we can see that at least some material is solid. The remaining crystal structure in each grain seems to be the stabilizing factor of the pore. However, until there is only vacuum between the powder, an observation of such pores is very rare and may eventually vanish over time.

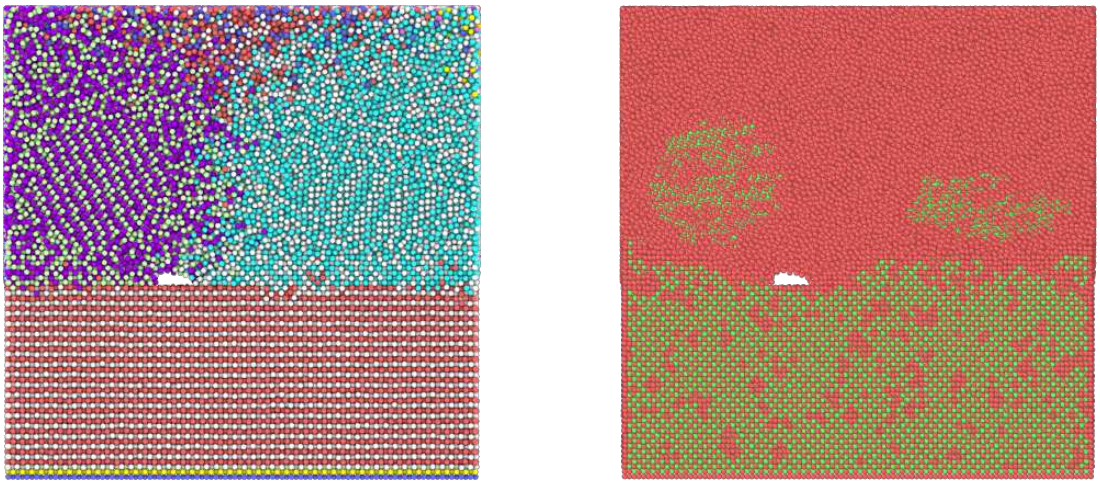

Figure 4.22: A small pore between two molten grains. Left: The original figure with the pore in more detail. Right: The same but colorized in terms of lattice structure.

5 Discussion

This chapter discusses the results of the LPBF simulations shown in chapter 4. We start by covering the limitations and opportunities for improvement. Afterwards we discuss results for particular simulations.

In contrast to real LPBF, we have to scale processing parameters such as time and laser power in MD simulations due to computational limitations. This however, makes it not easy to depict the highly non-linear material dynamics in a meaningful manner. Since we are limited in computational possibility, we have to find reasonable approaches for relations between real processing and simulation parameters. Therefore, section 4.3.1 introduced a for a more demanding powder bed which offers the possibility of further investigations into this. Although we included several important physical aspects to our samples, we neglected the size distribution of real powders for practical reasons and constructed all powder grains as spheres of same diameter. Therefore, an improvement which includes a meaningful size distribution is expected to increase the quality of simulations even further.

For the purpose to improve the implementation of the laser interaction, section 2.3.5 introduced a novel approach to have a density dependent absorption coefficient. We validate the implemented modifications to justify their usage in simulations. Therefore, we look at the injected laser energy during a simulation for a step shaped aluminium configuration. We show that the modifications for the absorption coefficient lead to the expected behavior of being density and material dependent. The modifications make it easy to turn off the laser interaction for certain materials which is, e.g., necessary when including a protective gas into the system. While working on this thesis we noticed a great potential to improve the laser implementation, which is the integration of a material dependent reflectance. This however, is only necessary when dealing with multi materials like binary alloys. Anyhow, until there is no ray tracing method integrated, the laser implementation remains improvable.

Coating material comparison

In section 4.1 we compared different material distribution configurations to study their suitability for LPBF. The presented configurations include a titanium coated aluminium core, an aluminium coated titanium core and a γ-TiAl sphere. Each configuration was constructed with a 50 % aluminium proportion and placed on a fixed ground of non-movable atoms. We observe that the basic concept of the implemented laser interaction

is sufficient to study the melt, respectively vaporization behavior for these simulations and obtain a sufficient set of laser parameters for all grains to melt completely.

For the processing of TiAl via electron-beam melting Cormier et al. reports an aluminium vaporization of approximately 6.1 % [35]. In contrast to that we have an aluminium reduction of 34.6 %, although we don't calculate the vaporized proportion but the reduction in terms of leftover melt and hence, cannot compare it one to one. However, the elemental composition analysis shows meaningful agreement with their findings and we are left with less aluminium than titanium due to its increased vaporization. For the titanium core, coated with aluminium we come closest to experimental measurements and calculate a change in the composition of 7.2 % in favor of titanium, whereas Cormier et al. measured 7.30 %, even though they started with a slightly different composition which also includes 4.06 % of other elements.

We show that the material configuration in terms of coated cores influences the behavior of the final composition a lot and yield an almost balanced titanium to aluminium composition when protecting an aluminium core with a titanium shell, even though the mixing is qualitatively not sufficient enough to result in the single phase γ-TiAl. We therefore suggest to extend the idea of coated cores up to multiple coatings, which is expected to increase the mixing and has the benefit of less aluminium vaporization and a more stable material composition. Future works could also adjust processing conditions and increase the initial aluminium content, which is expected to result in the desired single phase γ-TiAl [35].

Even if we don't reach the single phase γ-TiAl for the coated powder grains, a deeper investigation would be beneficial and could lead to usable applications, because suitable coatings can improve the final parts properties [11]. An alternating composition of α_2 and γ lamellar microstructures is even known to improve high-temperature creep resistance [36, 37]. Additionally, coated powders can improve the processability in terms of higher flowability and absorbance [11]. Although we don't use material dependent reflectances in our simulations, we observe differences in the processing for coated powders and thus, could improve processability by further research. However, material dependence is desirable and should be integrated for further investigations.

Laser speed comparison

In section 4.1.2 we compared the influence of the laser scanning speed for single γ-TiAl grains qualitatively and showed to have total different behavior in the material dynamics for changing laser speed. The formations we see are flower-like splashes as well as single splashing fountain that eventually shooting out a large droplet. We can see the expected attenuation of melting as the laser speed increases. This attenuation is due to the energy density decreasing when other parameters are held constant. For a detailed study of this behavior, [9, 10] can be consulted.

LPBF of γ-TiAl powder

In section 4.3.3 we investigated the new approach of a more demanding powder bed with γ-TiAl gains and analyzed the system by a measurement series that varies the laser power. We find simulation parameters that results in the expected behavior of a complete powder melting along the laser scanning trace surrounded by solid parts. We study the temperature profile and molten fractions during the simulation progress and find meaningful behavior such as recrystallization and heat conduction.

The boiling temperatures for aluminium and titanium are 2743 K and 3533 K [38] and have not been reached for these simulations. Therefore, vaporization is negligible and we classify the chosen parameters to resemble conduction mode. Especially for conduction mode in laser welding the vaporization of metals is considered to be negligible [15, 16] and therefore, we argue to have a good depiction of the expected behavior.

LPBF of mixed Ti-Al powder

In 4.3.4 we investigated LPBF simulations of a mixed Ti-Al powder, which consists of an alternated mixing of aluminium and titanium grains. The simulations show an increased melting of aluminium grains, whereas titanium grains remained more solid. This is of course expected, due to the different melting points of 933 K and 1943 K for aluminium and titanium [39].

The temperature profile shows a heating of some aluminium grains above 3000 K, and therefore, the vaporization of aluminium is increased. Despite increasing vaporization and temperatures above boiling point we observe few vaporized atoms and therefore classified the chosen parameters to also resemble conduction mode. The temperature profile supports this claim, because we have a decreasing temperature of hottest grains below boiling point.

Heat conduction is expected and was a requirement for the chosen powder configuration. We observe it in temperature profile and molten fraction analysis. Due to the heat conduction from aluminium to titanium grains, some titanium grains gain enough energy to increase melting, even after the laser left the sample. However, all grains are same in size and therefore heat conduction may bring other interesting findings when changing the size distribution.

Observable defects

We observed a tiny pore for a particular simulation. Although the pore is not surrounded by material completely, we identify it as an irregular cavity. The observation of such tiny vacuum pores is in fact not easy and need some stabilizing environment. However, to study the formation and prevention of defects in more detail, a protective gas has to be included into the system. Research in this regard is currently underway with aluminum

powders [10, 40], but could be extended to binary systems such as the present γ-TiAl alloy.

6 Conclusions and future work

Computer simulations offer an efficient way to investigate material dynamics and gain knowledge of quality-reducing properties. Further, they allow to investigate the suitability of new material and study functionalizing techniques such as powder coatings. Due to its attractive properties, γ-TiAl is used for demanding areas and high-temperature applications. However, the fabrication of γ-TiAl components by conventional methods is very difficult due to its physical properties and thus, laser powder bed fusion is an attractive alternative.

This thesis presented a molecular dynamics study on laser powder bed fusion of γ-TiAl which includes the analysis of single γ-TiAl grains, coated powder grains, as well as enlarged powder beds with a set of same sized powder grains. Thereby, a modification on the absorption coefficient to include material and density dependence provides meaningful results and a simulation model higher in quality. One finding is that the laser scanning speed does not only influence the energy density and hence, the molten fraction but also the material dynamics in term of splashing melt formation. Further, we have shown that observation of pores in vacuum is difficult because a stabilizing environment is necessary for vacuum cavities not to vanish.

The simulation results confirm an increased aluminium vaporization for the processing of titanium aluminide. Due to the increased vaporization of aluminium, we expect the γ-TiAl powder to reach a balanced composition if the initial aluminium content is increased accordingly. Another finding is that different configurations in terms of coated cores lead to different behavior and final elemental compositions. Thus, suitable coatings can improve mechanical properties and processability. For the configurations tested, titanium coatings can be used to decrease aluminium evaporation and hence, improve productivity.

The simulations with a demanding powder bed showed the desired behavior of a molten trace surrounded by solid material. This made it possible to analyze the melting processes during the simulation and observe heat conduction. With a suitable choice of laser parameters, melting of the substrate is achieved, which is necessary for the connection in additive manufacturing. In contrast to other simulations, the evaporation of aluminum is negligible. Therefore we classify presented simulations to resemble conduction mode melting. The simulations with mixed powder of aluminum and titanium grains showed an increased aluminum melting and achieved complete aluminum melting with the same simulation parameters. Unless the laser power is not increased further, the amount of vaporized aluminium also remains negligible and thus, resemble conduction mode.

In future work, we want to further investigate and integrate material dependent reflectances. Further, we want to study the influence of initial aluminium content for TiAl processing and investigate the functionalizing effect of coatings in more detail by changing properties and materials. Therefore, we will enlarge used powder beds even more and add a meaningful size distribution to the powder grains.

A Appendix

A.1 Colorized version of the mixed powder

Here we present a colorized version of the mixed powder from 4.3.4. The figures A.1, A.2 and A.3 show the final simulation state after 200 ps from different view angles. As in section 4.3.4 we cutted the sample in half for the front view A.2 and left side view A.3. Apart from a better differentiation of individual powder grains, there are no advantages for the examination.

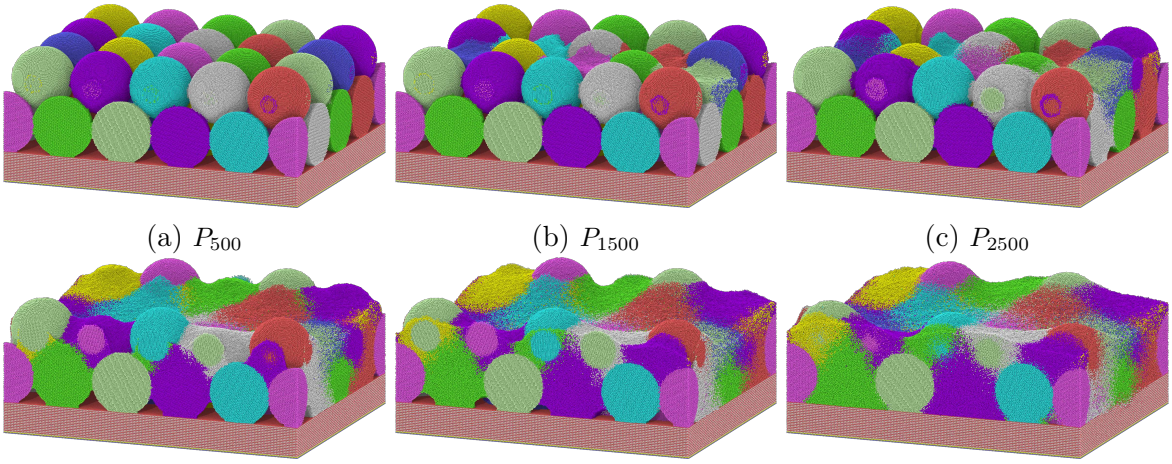

(a) P_{500} (b) P_{1500} (c) P_{2500}

(d) P_{3500} (e) P_{4500} (f) P_{5500}

Figure A.1: Colorized perspective views at $t = 200\,\text{ps}$ for the power series of mixed powder.

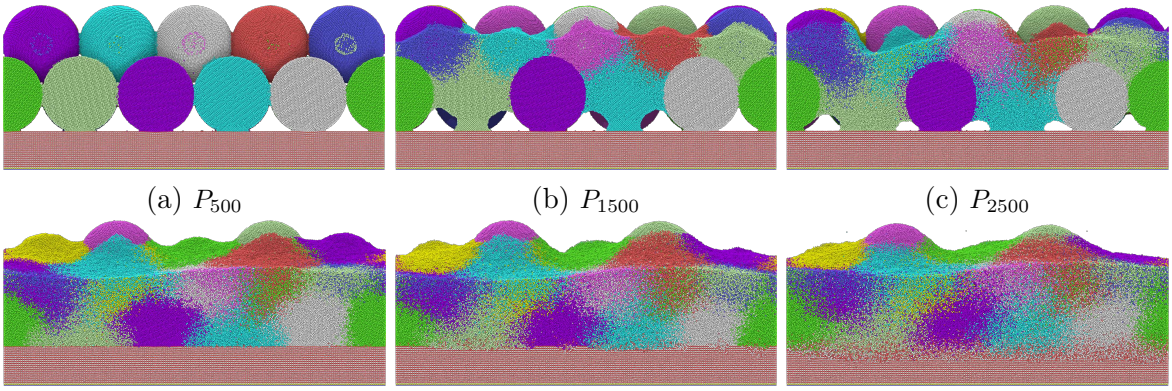

(a) P_{500} (b) P_{1500} (c) P_{2500}

(d) P_{3500} (e) P_{4500} (f) P_{5500}

Figure A.2: Colorized front views at $t = 200\,\text{ps}$ for the power series of mixed powder.

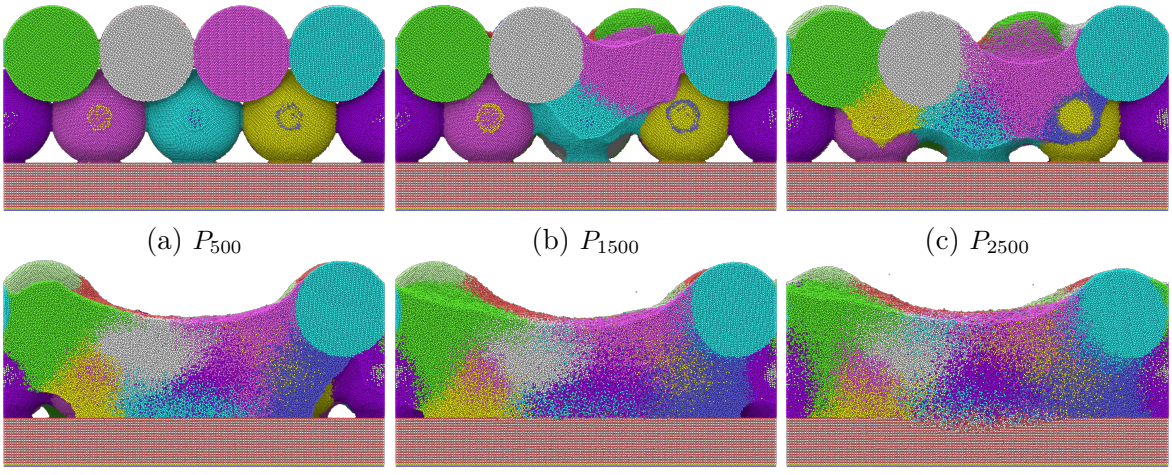

(a) P_{500} (b) P_{1500} (c) P_{2500}

(d) P_{3500} (e) P_{4500} (f) P_{5500}

Figure A.3: Colorized left side views at $t = 200\,\text{ps}$ for the power series of mixed powder.

A.2 IMD parameter file

The following is a content for parameter file which can be used for simulations of LPBF with IMD. It requires the explained modifications, which have been implemented. The meaning of individual parameters can be found in the documentation of IMD.

```
# I/O parameters
coordname                 equilibrated.config
outfiles                  lpbf

# main control parameters
simulation                1
ensemble                  nve
maxsteps                  200000
timestep                  0.1
ntypes                    2
total_types               84
pbc_dirs                  1 1 0
starttemp                 0.025851
box_from_header           1
checkpt_int               5000
eng_int                   1

# parameters for EAM
core_potential_file       TiAl_pair_imd.dat
embedding_energy_file     TiAl_embed_imd.dat
atomic_e-density_file     TiAl_rho_imd.dat

# make (virtual) atoms unmovable
restrictionvector         2 0 0 0
restrictionvector         3 0 0 0

# parameters for LASER option
laser_rescale_mode        3
laser_steps               16000
laser_mu_vol              0.042 0.098
laser_fwhm                320
laser_start_position      -400 320
laser_velocity            1.0 0.0
laser_reflectivity        0.61511
laser_power               3897.2
```

A.3 Make config parameter file

For the purpose of creating atoms configurations, a little tool has been developed. The tiny program can take parameters as command-line arguments or read the parameters from a file. A proper content of such a file is listed below, which creates the configuration shown in figure 3.2d and may be executed as

`make_config --set -o outfile --parse paramfile`

A documentation of the parameters is available within program itself by executing it with `--help`.

```
--set -p

--set -l L1_0 -a 3.997 -c 4.062 -t 0 1 -m 47.867 26.981
--init -S 800.0 400.0 435.0
--add -t 0 1 -select reset -select below 800.0 400.0 15

--set -S 400.0 400.0 400.0

--add -t 2 3
-rotate 200.0 200.0 200.0 random
-shift 0.0 0.0 15.0
-select reset
-select in sphere 200.0 200.0 215.0 200.0

--add -t 4 5
-rotate 200.0 200.0 200.0 random
-shift 400.0 0.0 15.0
-select reset
-select in sphere 600.0 200.0 215.0 200.0
```

A.4 German summary

Neue Anwendungen im Bereich additiver Fertigung erfordern eine ständige Steigerung von Qualität und Produktivität [1]. Eine Methode um dies zu erlangen sind neue, anspruchsvollere Materialien. Titanaluminide weisen attraktive Eigenschaften auf. In dieser Arbeit untersuchen wir γ-TiAl, welches seine mechanischen Eigenschaften auch unter hohen Temperaturen aufrecht erhalten kann [4] und daher in Bereichen wie der Luft- und Raumfahrt eingesetzt wird [2]. Die positiven Eigenschaften von γ-TiAl machen eine Bearbeitung mit herkömmlichen Verfahren allerdings schwierig [5]. Die additive Fertigung stellt daher eine vielversprechende Methode zur Herstellung von γ-TiAl Werkstücken dar [6].

In dieser Arbeit untersuchen wir die additive Fertigung von γ-TiAl durch *Laser Powder Bed Fusion (LPBF)*. Dies ist ein Fertigungsverfahren, welches üblicherweise zur additiven Fertigung von Metallen verwendet wird. Dabei untersuchen wir die physikalischen Prozesse mithilfe Molekulardynamik-Simulationen, welches auf dem iterativen Lösen der Newtonschen Bewegungsgleichungen basiert. Hierdurch erhalten wir die zeitliche Entwicklung des Systems und können unter anderem das Schmelz- und Verdampfungsverhalten analysieren. Weiterhin sind wir hierdurch in der Lage, Strukturen und deren elementare Eigenschaften auf atomistischer Skala zu untersuchen.

Ein besonderes Interesse dieser Arbeit gilt beschichteten Ti-Al-Systemen. Das wird dadurch begründet, dass beschichtete Materialien verbessernde Eigenschaften besitzen können und die Verarbeitung mit LPBF erleichtern können [11]. Deshalb analysieren wir Beschichtungen des Ti-Al-Systems und vergleichen deren Verhalten mit γ-TiAl Pulverpartikeln. Außerdem erhöhen wir die Anzahl der Pulverpartikel bisheriger Simulationen um ein möglichst realitätsnahes Pulverbett zu simulieren. Dadurch haben wir die Möglichkeit das Verhalten des Schmelzbades detaillierter zu untersuchen. Weiterhin stellen wir damit die notwendigen Voraussetzungen um weitere Forschung hinsichtlich der Korrelationen zu realen Prozessparametern zu untersuchen.

Eine erste Erkenntnis aus den Simulationsergebnissen ist der Einfluss der Lasergeschwindigkeit auf das Schmelzverhalten einzelner Pulverpartikel. Erwartungsgemäß sinkt der Schmelzanteil mit steigender Geschwindigkeit aufgrund der damit verbundenen Reduzierung der Energiedichte. Zusätzlich beobachten wir den Einfluss der Geschwindigkeit auf die Form der Schmelzspritzer. Die Anzahl der Spritzer sinkt mit steigender Geschwindigkeit bis hin zu einer fontänenartigen Ablösung eines großen Schmelztropfens.

Die LPBF Simulationen am Ti-Al-System bestätigen eine erhöhte Aluminiumverdampfung während der Bearbeitung. Durch eine Erhöhung des Aluminiumanteils im Pulver könnte die gewünschte γ-TiAl-Phase erreicht werden. Eine weitere Erkenntnis ist, dass Beschichtungen Einflüsse auf die elementare Zusammensetzung haben. Wir bestätigen daher, dass Beschichtungen die mechanischen Eigenschaften verbessern können. Insbesondere hat sich gezeigt, dass Titanbeschichtungen für eine Verringerung der Alu-

miniumverdampfung genutzt werden können und sich dadurch die Produktivität steigern lässt.

In den Simulationen mit einem anspruchsvolleren Pulverbett zeigte sich das gewünschte Verhalten einer geschmolzenen Spur, welche von fest gebliebenem Material umschlossen ist. Dadurch konnten die Schmelzverläufe während der Simulation analysiert und Wärmeleitung beobachtet werden. Bei geeigneter Wahl an Laserparametern wird ein Anschmelzen des Substrates erreicht, welches für eine gute Verbindung bei der additiven Fertigung notwendig ist. Im Gegensatz zu anderen Simulation ist die Verdampfung von Aluminium jedoch vernachlässigbar, weshalb wir die Simulationen als *Conduction Mode Melting* einstufen. Die Simulationen mit gemischtem Pulver aus Aluminium- und Titanpartikeln zeigten ein gesteigertes Schmelzen zugunsten der Aluminiumpartikel. Bei gleichen Simulationsparametern wird ein vollständiges Aufschmelzen von Aluminium erreicht. Die Temperatur bleibt jedoch weitestgehend unterhalb der Siedepunkte und der Anteil an verdampftem Aluminium bleibt vernachlässigbar.

Im Zuge dieser Arbeit wurde das verwendete Simulationsprogramm erweitert um eine material- und dichteabhängige Absorption der Laserleistung zu ermöglichen. Die Anpassungen werden durch physikalische Eigenschaften legitimiert und deren Umsetzung mithilfe einer Referenzsimulation untersucht. Die Ergebnisse zeigten das gewünschte Verhalten einer dichteabhängigen Absorption und rechtfertigen die Verwendung in weiteren Simulationen. Auch wenn mit den Änderungen die Qualität der Simulationen gesteigert werden konnte, lässt sich das aktuelle Modell noch weiter verbessern. Das größte Verbesserungspotential sehen wir aktuell in der fehlenden Materialabhängigkeit der Reflektivität.

In zukünftigen Arbeiten wollen wir die Untersuchungen von metallischen Legierungen vertiefen und eine materialabhängige Reflektivität in unsere Simulationen integrieren. Weiterhin wollen wir den Aluminiumgehalt der Pulverpartikel variieren und die Untersuchungen der funktionellen Effekte von Materialbeschichtungen vertiefen. Dazu werden wir bisherige Simulationen weiter vergrößern und eine realitätsnahe Größenverteilung der Pulverpartikel verwenden.

Bibliography

[1] Sarah Müller and Engelbert Westkämper. "Modelling of Production Processes: A Theoretical Approach to Additive Manufacturing." In: *Procedia CIRP* 72 (2018). 51st CIRP Conference on Manufacturing Systems.

[2] Giorgio Baudana et al. "Titanium aluminides for aerospace and automotive applications processed by Electron Beam Melting: Contribution of Politecnico di Torino." In: *Metal Powder Report* 71.3 (2016).

[3] Helmut Clemens and Wilfried Dr. Smarsly. "Light-Weight Intermetallic Titanium Aluminides – Status of Research and Development." In: *Advanced Materials Research* 278 (2011).

[4] Anıl Emiralioğlu and Rahmi Ünal. "Additive manufacturing of gamma titanium aluminide alloys: a review." In: *Journal of Materials Science* 57.7 (Feb. 1, 2022).

[5] Bo-chao Lin and Wei Chen. "Mechanical properties of TiAl fabricated by electron beam melting — A review." In: *China Foundry* 18.4 (July 1, 2021).

[6] Ozge Genc and Rahmi Unal. "Development of gamma titanium aluminide (γ-TiAl) alloys: A review." In: *Journal of Alloys and Compounds* 929 (2022).

[7] Ruihu Zhou, Haisheng Liu, and Huifu Wang. "Modeling and simulation of metal selective laser melting process: a critical review." In: *The International Journal of Advanced Manufacturing Technology* 121.9 (Aug. 1, 2022).

[8] Dominic Klein. "Laser Ablation of Covalent Materials." PhD thesis. Institute for Functional Matter and Quantum Technologies, Apr. 2023.

[9] Fabio Oelschläger. "Molekulardynamische Simulation von selektivem Laserschmelzen." Bachelor's Thesis. Institut für Funktionelle Materie und Quantentechnologien, Apr. 30, 2021.

[10] Azad Gorgis. "Simulation Studies of Selective Laser Melting." MA thesis. Institute for Functional Matter and Quantum Technologies, Sept. 1, 2022.

[11] Robert Bidulsky et al. "Coated Metal Powders for Laser Powder Bed Fusion (L-PBF) Processing: A Review." In: *Metals* 11.11 (2021).

[12] Günther Poszvek et al. "Fused Filament Fabrication of Metallic Components for Semi-professional and Home Use." In: *Digital Conversion on the Way to Industry 4.0*. Ed. by Numan M. Durakbasa and M. Güneş Gençyılmaz. Cham: Springer International Publishing, 2021.

[13] D. B. Hann, J. Iammi, and J. Folkes. "A simple methodology for predicting laser-weld properties from material and laser parameters." In: *Journal of Physics D: Applied Physics* 44.44 (Oct. 2011).

[14] D. B. Hann, J. Iammi, and J. Folkes. "Keyholing or Conduction – Prediction of Laser Penetration Depth." In: *Proceedings of the 36th International MATADOR Conference*. Ed. by Srichand Hinduja and Lin Li. London: Springer London, 2010.

[15] Sagar Patel and Mihaela Vlasea. "Melting modes in laser powder bed fusion." In: *Materialia* 9 (2020).

[16] J. C. Ion, H. R. Shercliff, and M. F. Ashby. "Diagrams for laser materials processing." In: *Acta Metallurgica et Materialia* 40.7 (1992).

[17] Bi Zhang, Yongtao Li, and Qian Bai. "Defect Formation Mechanisms in Selective Laser Melting: A Review." In: *Chinese Journal of Mechanical Engineering* 30.3 (May 1, 2017).

[18] Sam Coeck et al. "Prediction of lack of fusion porosity in selective laser melting based on melt pool monitoring data." In: *Additive Manufacturing* 25 (2019).

[19] Haijun Gong et al. "Melt Pool Characterization for Selective Laser Melting of Ti-6Al-4V Pre-alloyed Powder." In: *25th Annual International Solid Freeform Fabrication Symposium*. Aug. 2014.

[20] Ming Tang, P. Chris Pistorius, and Jack L. Beuth. "Prediction of lack-of-fusion porosity for powder bed fusion." In: *Additive Manufacturing* 14 (2017).

[21] Jonas Schmid. "Molecular dynamic simulation of 3D Laser Printing." In: *Master's thesis*. 2023.

[22] Wolfgang Nolting. *Grundkurs Theoretische Physik 3*. 10th ed. Springer Spektrum Berlin, Heidelberg, Oct. 22, 2013.

[23] Mikhail N. Polyanskiy. *Refractive index database*. Ed. by Mikhail N. Polyanskiy. 2023. URL: `https://refractiveindex.info`.

[24] Aleksandar D. Rakić et al. "Optical properties of metallic films for vertical-cavity optoelectronic devices." In: *Appl. Opt.* 37.22 (Aug. 1998).

[25] P. B. Johnson and R. W. Christy. "Optical constants of transition metals: Ti, V, Cr, Mn, Fe, Co, Ni, and Pd." In: *Phys. Rev. B* 9 (12 June 1974).

[26] Daan Frenkel and Berend Smit. *Understanding Molecular Simulation : From Algorithms to Applications*. San Diego, UNITED STATES: Elsevier Science & Technology, 2001.

[27] Murray S. Daw and M. I. Baskes. "Embedded-atom method: Derivation and application to impurities, surfaces, and other defects in metals." In: *Phys. Rev. B* 29 (12 June 1984).

[28] Johannes Roth et al. "IMD – the ITAP molecular dynamics simulation package." In: *The European Physical Journal Special Topics* 227.14 (Mar. 1, 2019).

[29] Rajendra R. Zope and Y. Mishin. "Interatomic potentials for atomistic simulations of the Ti-Al system." In: *Phys. Rev. B* 68 (2 July 2003).

[30] Wentian Shi et al. "Beam Diameter Dependence of Performance in Thick-Layer and High-Power Selective Laser Melting of Ti-6Al-4V." In: *Materials* 11.7 (2018).

[31] J. R. De Laeter et al. "Atomic weights of the elements. Review 2000 (IUPAC Technical Report)." In: *Pure and applied chemistry* 75.6 (2003).

[32] Alexander Stukowski. "Visualization and analysis of atomistic simulation data with OVITO-the Open Visualization Tool." In: *Modelling and Simulation in Materials Science and Engineering* 18.1 (Jan. 2010).

[33] Alexander Stukowski. "Structure identification methods for atomistic simulations of crystalline materials." In: *Modelling and Simulation in Materials Science and Engineering* 20.4 (May 2012).

[34] Norbert Lümmen and Thomas Kraska. "Common neighbour analysis for binary atomic systems." In: *Modelling and Simulation in Materials Science and Engineering* 15.3 (Mar. 2007).

[35] Denis Cormier et al. "Freeform Fabrication of Titanium Aluminide via Electron Beam Melting Using Prealloyed and Blended Powders." In: *Research Letters in Materials Science* 2007 (Jan. 31, 2008).

[36] Stephan S. A. Gerstl, Young-Won Kim, and David N. Seidman. "Atomic Scale Chemistry of $\alpha 2/\gamma$ Interfaces in a Multi-Component TiAl Alloy." In: *Interface Science* 12.2 (Apr. 1, 2004).

[37] S. Karthikeyan et al. "Mechanisms and effect of microstructure on creep of TiAl-based alloys." In: *Materials Science and Engineering: A* 329-331 (2002).

[38] Yiming Zhang. "Corrected Values for Boiling Points and Enthalpies of Vaporization of Elements in Handbooks." In: *Journal of Chemical & Engineering Data* 56 (Jan. 2011).

[39] Taylor & Francis Group. *Handbook of Chemistry and Physics*. Vol. 104. CRC Press, 2023.

[40] Fabio Oelschläger et al. "Atomistic simulations of laser powder bed fusion." In: Sept. 2023.

All links were lastly followed on September 23, 2023